J. Fluid Mech. (2012), *vol.* 704, *pp.* 5–36. © Cambridge University Press 2012
doi:10.1017/jfm.2012.141

Evolution of fluid-like granular ejecta generated by sphere impact

J. O. Marston†, E. Q. Li and S. T. Thoroddsen

Division of Physical Sciences and Engineering, King Abdullah University of Science and Technology, Thuwal 23955-6900, Saudi Arabia

(Received 11 July 2011; revised 27 February 2012; accepted 9 March 2012; first published online 1 May 2012)

We present results from an experimental study of the speed and shape of the ejecta formed when a solid sphere impacts onto a granular bed. We use high-speed imaging at frame rates up to 100 000 f.p.s. to provide direct measurement of individual grain velocities and ejecta angles as well as the overall evolution of the granular ejecta. For larger grain sizes, the emergence velocities of the grains during the 'early stage flow', i.e. before the main ejecta 'curtain' forms, increase with the kinetic energy of the impacting sphere but are inversely proportional to the time from impact. We also observe that the fastest grains, which can obtain velocities up to five times that of the impacting sphere ($V_g/V_0 = 5$), generally emerge at the earliest times and with the lowest ejection angles. As the grain size is decreased, a more 'fluid-like' behaviour is observed whereby the ejected material first emerges as a thin sheet of grains between the sphere and the bed surface, which is also seen when a sphere impacts a liquid pool. In this case, the sheet velocity is approximately double that of the impacting sphere ($V_s/V_0 = 2$) and independent of the bulk packing fraction. For the finest grains we provide evidence of the existence of a vortex ring inside the ejecta curtain where grains following the air flow are entrained through the curtain. In contrast to predictions from previous studies, we find that the temporal evolution of the ejecta neck radius is not initially quadratic but rather approaches a square-root dependence on time, for the finest grains with the highest impact kinetic energy. The evolution therefore approaches that seen for the crown evolution in liquid drop impacts. By using both spherical glass beads and coarse sands, we show that the size and shape distribution are critical in determining the post-impact dynamics whereby the sands exhibit a qualitatively different response to impact, with grains ejected at lower speeds and at later times than for the glass beads.

Key words: fluidized beds, granular media, jets

1. Introduction

The result of high-velocity projectile impacts onto loosely packed and densely packed surfaces, pertaining to impact cratering, is a complex process and perhaps poorly understood due to the inherently short time scales involved in such high-speed events. Numerous insightful experiments into this rich phenomenon have involved solid-body impacts onto a relatively loosely packed granular medium some of which are discussed below, however, for a thorough overview of the scalings involved in ejecta and cratering processes, the reader is referred to Holsapple (1993) and Housen

† Email address for correspondence: jeremy.marston@kaust.edu.sa

https://doi.org/10.1017/jfm.2012.141 Published online by Cambridge University Press

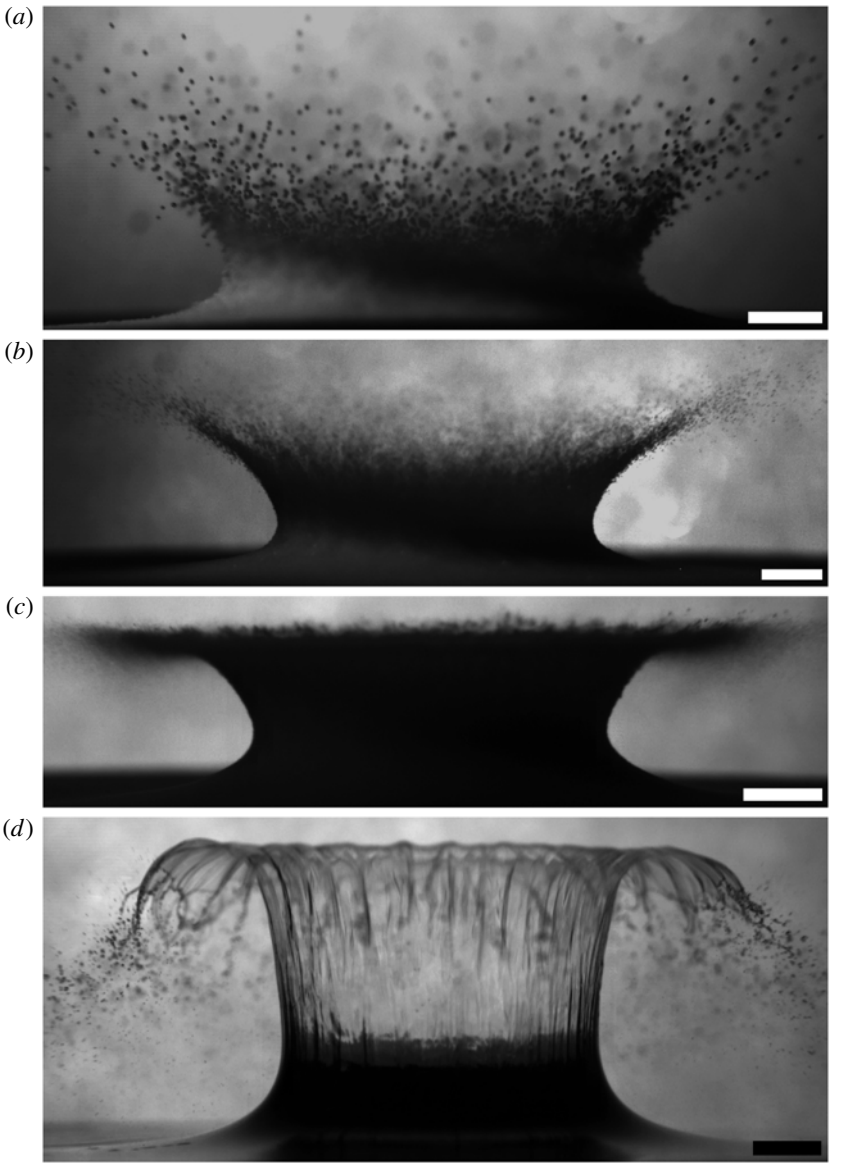


FIGURE 1. Images taken from high-speed video sequences showing the ejecta produced by the impact of a solid sphere onto different targets: (*a*) 520 μm glass beads ($\phi = 0.59$), (*b*) 178 μm glass beads ($\phi = 0.58$), (*c*) 31 μm glass beads ($\phi = 0.49$) and (*d*) water ($Re = 2.44 \times 10^5$). For all cases, the impact velocity $V_0 = 9.8$ m s^{-1} and the sphere diameter $D_0 = 25$ mm, corresponding to a Froude number $Fr = 19.8$ and density ratios $\varrho = 5.3$, 5.35, 6.37 and 7.85. Each image is taken at 5.7 ms from first contact and the scale bars represent 1 cm. See also supplementary video 1 available at journals.cambridge.org/flm.

& Holsapple (2011). Figure 1 shows snapshots of the ejecta generated by the impact of a solid sphere onto different media. The first three images show impacts onto granular beds with decreasing grain sizes while the last image is the case for water used as a reference.

https://doi.org/10.1017/jfm.2012.141 Published online by Cambridge University Press

A fundamental question pertaining to many different granular flow configurations is, under what conditions can the granular material exhibit fluid-like behaviour? Here, we address this question in the context of the events occurring immediately after impact onto a static granular bed. Specifically, can the quantitative behaviour of the ejecta formed exhibit fluid-like characteristics?

Thoroddsen & Shen (2001) reported observations of a granular jet which emerges from below the surface following the impact of a solid sphere onto a loose granular bed. In this case, the jet results from the collapse of the cavity formed during the sphere penetration. In a sense, this can be considered the granular equivalent of the well-known Worthington jet seen when a liquid drop impacts a liquid pool. Along with this observation, various other flow configurations have been implemented to study the analogy between a granular medium and a fluid during impact phenomena such as the 'granular jump' (Boudet *et al.* 2007) when a constant flow of granular material impacts a horizontal plate and the equivalent 'water bell' experiments (Cheng *et al.* 2007). A freely falling granular jet has also been shown to exhibit 'break-up' or clustering patterns similar to those seen in surface tension-driven break-up of liquid jets (Mobius 2006; Eggers & Villermaux 2008; Royer *et al.* 2009). Regarding the mechanisms responsible for these apparent similarities between granular material and liquids, Royer *et al.* (2009) show that short-range cohesive forces, arising from van der Waals interactions, and minute capillary bridges due to ambient moisture are significant in determining the dynamical behaviour of the flow.

Specific to solid-body impacts onto granular surfaces, focal points of numerous studies have included the shape and size of the crater formed on the powder surface (e.g. Walsh *et al.* 2003; de Vet & de Bruyn 2007), the penetration depth of the sphere (e.g. Uehara *et al.* 2003; Ambroso *et al.* 2005) the deceleration of the sphere (Goldman & Umbahnowar 2008), the energy transfer coefficient from the impactor to the granular ejecta and velocity distributions (e.g. Hartmann 1985; Yamamoto *et al.* 2005; Beladjine *et al.* 2007; Colwell *et al.* 2008) and the dynamics of the jet with the influence of packing and ambient pressure (Lohse *et al.* 2004; Caballero *et al.* 2007; Royer *et al.* 2007; Marston *et al.* 2008; Royer *et al.* 2008; von Kann *et al.* 2010).

In contrast, relatively little attention has been paid to the evolution and dynamics of the granular ejecta curtain. Yamamoto *et al.* (2006) examined the transient crater growth following the impact of a projectile into glass beads, however their framing rate of 30 f.p.s. did not allow them to obtain early time data. For impacts onto shallow layers, Boudet, Amarouchene & Kellay (2006) presented a simple kinematic model of the corona shape based upon the initial speed of the disturbance to the grains and an effective shear in the bed. For deeper beds the ejecta angle, α, was measured by Deboeuf, Gondret & Rabaud (2009) to be approximately constant in time with $\alpha \sim 56^\circ$. In their analysis, they fit their data to a ballistic model and find that the growth of the neck of the ejecta is quadratic in time. Both models assume that the grains are ejected at a single angle at a given time. The experiments used in fitting to these models are hampered somewhat by the temporal resolution of their experiments (up to 2000 and 500 f.p.s., respectively) which did not permit observations of the ejecta shapes at early times nor of the motion of the first grains ejected from the bed.

The overall objective of this paper is therefore to use high-speed imaging with frame rates up to 100 000 f.p.s. corresponding to time intervals $\Delta t = 10$ μs to focus on the early time dynamics, $t \leqslant 10$ ms, of the post-impact phenomena such as grain ejection and the associated ejecta angles and speeds and the early time evolution of the ejecta neck.

https://doi.org/10.1017/jfm.2012.141 Published online by Cambridge University Press

2. Experimental set-up

2.1. *Setup geometry*

For our experiments, stainless steel spheres with diameters $D_0 = 20$, 25, 38 and 50 mm and density $\rho_0 = 7850$ kg m^{-3} were released using an electromagnet from a specified height, $0.03 \leqslant h_r \leqslant 13$ m, above the centre of a granular bed. This range of impact heights yielded a range of sphere impact velocities $0.78 \leqslant V_0 \leqslant 16$ m s^{-1}, which was measured directly from the video clips. The target bed was placed inside of an open-top containment box with a viewing window at the front for direct imaging and a diffuser screen at the rear to produce uniform back-lighting for silhouette imaging.

The container itself was a stainless steel pot with inner diameter 20 cm and height 10 cm and capacity of 3.14 litres. Although the effects of confinement have been shown to influence the dynamics of the sphere within the bed (Goldman & Umbahnowar 2008; Seguin, Bertho & Gondret 2008), here we are focusing on events above the granular surface at early times, usually within several milliseconds from impact so that the sphere penetration depth, $H \leqslant tV_0 < 2D_0$, therefore during the time frame for most of the events which we analyse, the sphere has yet to reach the bottom of the container.

All experiments were carried out in an air-conditioned laboratory at 21 °C and relative humidity of 55 %. As such, we cannot rule out the possible presence of small capillary forces due to liquid bridge formation between particles which may be more significant for the smallest grains (Royer *et al.* 2009), however the effect is minimized by maintaining constant ambient conditions throughout all of the experiments.

2.2. *Granular materials*

The target beds consisted of either spherical glass beads with diameters $d_b < 53$, 106–212 and 425–600 μm as stated by the manufacturer (Pan Abrasives Ltd, Singapore) or coarse sands. For the sands, two samples were tested, namely beach sand and Arabian desert sand. The beach sand was sieved with a 1 mm mesh size and the desert sand was sieved with a mesh size of 500 μm. Particle size and shape (circularity) analyses of these materials were performed on a combination of a Malvern Mastersizer and a Malvern Morphologi G3. As shown in table 1, the glass beads exhibit mono-modal size distributions for all three size ranges with volume-based mean diameters, $d_{4,3} = 31$, 178 and 520 μm, respectively, where

$$d_{4,3} = \frac{\sum_{i=1}^{n} d_i^4}{\sum_{i=1}^{n} d_i^3}. \tag{2.1}$$

We use this as the characteristic mean diameter for the glass beads, i.e. $d_b = d_{4,3}$. To characterize the shape, we use the Malvern high-sensitivity circularity measurement, $C_{HS} = 4\pi A/P^2$, where A is the cross-sectional area and P is the perimeter as determined by the Morphologi G3. For the glass beads, the mean circularity $C_{HS,mean} = 0.96$, showing that they are indeed nearly spherical. However, for the beach and desert sands $C_{HS,mean} = 0.41$ and 0.64, respectively, with corresponding ranges $(C_{HS,10}, C_{HS,90}) = (0.12, 0.8)$ and (0.28, 0.89) showing that these sands have a broad shape distribution. Since these sands are mostly non-spherical, we take surface-area-based mean diameters as the characteristic diameter, i.e. $d_b = d_{3,2} = 524$ and 301 μm for the beach and desert sands, respectively. The grain density is $\rho_g \approx 2500$ kg m^{-3}.

https://doi.org/10.1017/jfm.2012.141 Published online by Cambridge University Press

Material	d_{10}	d_{50}	d_{90}	$d_{3,2}$	$d_{4,3}$
Glass beads <53	19	30	46	28	31
Glass beads 106–212	127	174	234	169	178
Glass beads 425–600	441	493	564	515	520
Beach sand	202	490	899	524	
Desert sand	128	294	482	301	

TABLE 1. Characteristic diameters for the glass beads and sands. All values stated in μm.

Material	(*a*) Pour + scrape	(*b*) Press + scrape	(*c*) tap 1 min + scrape	(*d*) tap3 min + scrape
31 μm glass beads	0.49	0.55	0.58	0.61
178 μm glass beads	0.59		0.62	0.64
520 μm glass beads	0.59			0.63
Beach sand (<1 mm)	0.57			0.67
Desert sand (<500 μm)	0.59			0.68

TABLE 2. Solid volume fractions (packing fraction), ϕ, produced by different bed preparation methods.

2.3. *Bed preparation*

The beds were prepared by a variety of methods in order to assess the influence of the solids volume (packing) fraction, ϕ. We used four well-characterized methods in our preparation which yielded consistent and reproducible packings. The four methods, as shown in table 2, were (*a*) pouring, (*b*) pressing with a ∼15 kg plate, (*c*) tapping the container edge for 1 minute or (*d*) tapping the container edge for 3 min. In addition to each of the methods, the bed was scraped level to ensure impact onto a level surface. This additional scraping inherently alters the packing state in the very top layers of grains but did not affect the bulk packing. The first method (pour and scrape) has been used in previous studies (Thoroddsen & Shen 2001; Deboeuf *et al.* 2009), whilst the method of tapping can be used to measure 'tap porosity' in powder beds (Hapgood *et al.* 2002). The bed packing fraction was then deduced by the difference in mass between the filled and empty container. Using these different preparation methods, we were able to produce packing fractions in the range $0.49 \leqslant \phi \leqslant 0.68$ leading to bulk granular densities $1225 \leqslant \rho_b \leqslant 1700$ kg m^{-3}.

2.4. *Parameter space*

Relevant dimensionless parameters for this study include the Froude number, density ratio, size ratio and relative size distribution factor:

$$Fr = \frac{V_0}{\sqrt{gD_0}}, \quad \varrho = \frac{\rho_0}{\rho_b}, \quad \epsilon = \frac{D_0}{d_b}, \quad \Delta S = \frac{d_{90} - d_{10}}{d_{50}} \tag{2.2}$$

where the bulk density of the bed, $\rho_b = \phi\rho_g$ where ϕ is the solids packing fraction and $\rho_g \approx 2500$ kg m^{-3} is the individual grain density. As such, for our

https://doi.org/10.1017/jfm.2012.141 Published online by Cambridge University Press

experiments, $0.49 \leqslant \phi \leqslant 0.68$, $4.6 \leqslant \varrho \leqslant 6.4$, $1.5 \leqslant Fr \leqslant 32$, $38 \leqslant \epsilon \leqslant 1600$ and $0.25 \leqslant \Delta S \leqslant 1.42$. One might also invoke a modified form of the Reynolds number (e.g. Thoroddsen & Shen 2001), however, we reserve discussion of this until later (§ 8.1). Since all of the experiments were conducted at ambient air pressure, the role of air drag warrants some discussion here; the particle Reynolds number of an individual grain is given by

$$Re_g = \frac{d_b V_g \rho_{air}}{\mu_{air}}, \tag{2.3}$$

where ρ_{air} and μ_{air} are the air density and viscosity, respectively. As such, for the largest grains $d_b = 520$ μm ejected at the highest speeds found herein $V_g = O(30)$ m s^{-1}, we have $Re_g = O(10^3)$ and a drag coefficient, $C_d = 0.44$. The typical deceleration due to the air drag in this instance can then be approximated as

$$a^* \approx \frac{\rho_{air} V_g^2}{3 d_b \rho_g} \tag{2.4}$$

yielding decelerations as high as $a^* \approx 30$ g. The form of the drag coefficient will of course vary depending on the grain size (and shape) and ejection speed, but this calculation shows that the air drag may be significant for the fastest grains. We note, however, that the velocity of an ejected grain is only appreciably reduced by air drag over a distance L_{drag} during which the ejected grain encounters its own mass (Hartmann 1985) given by

$$L_{drag} = \frac{4 d_b \rho_g}{6 \rho_{air}}. \tag{2.5}$$

As such, we find drag lengths $L_{drag} = 4$ cm for the finest grains ($d_b = 31$ μm), however for the larger grains $L_{drag} \geqslant 25$ cm which is larger than the distance over which we track the grains for velocity measurements. Thus, we expect the role of air to be significant for the finest grains but for the large grains ($d_b \geqslant 178$ μm) even for atmospheric pressure we can neglect the influence of air drag on the ejecta velocity measurements within our field of view.

2.5. *Image capture and analysis*

The impact and subsequent ejecta evolution were imaged using a high-speed video camera (Photron Fastcam SA-5) equipped with a Nikon 60 or 105 mm micro-lens at frame rates from 7500 up to 100 000 f.p.s. yielding time steps $\Delta t \geqslant 10$ μs. The recording duration was sufficient to allow for manual triggering. Back-lighting, to yield silhouette images, was achieved using several 350 W Sumita metal halide light sources with an additional side-light illuminating the surface to identify the exact point of impact.

From the video sequences, it was then possible to measure a variety of basic features including the impact velocity, V_0, the sphere penetration depth, $H(t)$ for $H \geqslant -0.8 D_0$, the emergence radius, r_e, and time, t_e, where the grains (or sheet) first emerge. Individual grain velocities, V_g, and ejection angles, α_g, were determined by tracking individual grains frame by frame from first emergence to the edge of the field of view. Throughout this part of the grain's trajectory, the motion is a straight line from the point of ejection with a constant velocity. In addition, image sequences were analysed using Davis 7.2 software (LaVision GmbH) to generate streak images of the particle trajectory at given times from impact. By measuring the length and elevation

https://doi.org/10.1017/jfm.2012.141 Published online by Cambridge University Press

of these streaks, we were able to determine the particle velocity (i.e. ejecta speed and angle). The use of a micro-lens renders a narrow depth of field so the measurement plane is established optically and we discount the measurements of particles with out-of-plane motion.

The spatiotemporal evolution of the ejecta and specifically the ejecta neck (defined as the minimum distance to the sphere's axis of symmetry) was determined using a custom-written routine in Matlab. An example sequence of an impact is shown in figure 2(*a*) for $D_0 = 38$ mm, $V_0 = 9.05$ m s^{-1}, $d_b = 178$ μm and figure 2(*b*) shows the corresponding extracted shape of the ejecta at different times using this routine. In addition, figure 2(*c*) shows graphical definitions of r_e, the emergence radius, and r_n, the instantaneous neck radius, for $D_0 = 38$ mm, $V_0 = 16$ m s^{-1} and $d_b = 31$ μm.

3. Qualitative features of granular impact

Figure 3 shows images taken from a video sequence captured at 30 000 f.p.s. for the impact of a $D_0 = 38$ mm sphere onto a bed of spherical glass beads with $d_b = 520$ μm. In this particular realization, the impact velocity $V_0 = 4.62$ m s^{-1} ($Fr = 7.6$) and the initial packing fraction $\phi = 0.59$ ($\varrho = 5.3$). The main features shown are the moment of impact (image 1, $t = 0$), the emergence radius at the emergence time (image 2, $t = t_e = 1.3$ ms), the formation of the ejecta neck (image 3, $t = 5.3$ ms), the growth of the ejecta (image 4, $t = 8.5$ ms), the maximum height of the ejecta neck (image 5, $t = 19.1$ ms) and the formation of a corner at the neck during the collapse stage (images 6 and 7, $t = 51.5$ and 89.1 ms). In image 7, the ejecta edge makes an approximate 57° angle with the bed surface, similar to the angles measured by Deboeuf *et al.* (2009), but we note that this angle is only well defined once this corner has formed in the latter stages of the ejecta evolution. The zoomed imaged on the right shows discrete grains which can be tracked throughout the field of view from which we can determine the grain trajectory and speed.

Figure 4 shows image sequences taken from six high-speed video clips taken at 30 000 f.p.s. Here, we show three different granular materials (glass beads $d_b = 31$ μm, glass beads $d_b = 178$ μm and desert sand $d_b = 301$ μm) each with two different bed preparations (pour and scrape or tap for 3 min). The impact velocity ($V_0 = 4.63$ m s^{-1}) and sphere diameter ($D_0 = 38$ mm) were the same for each trial yielding $Fr = 7.6$ for these realizations. The differences in the physical appearance of the ejecta are quite stark for these cases, highlighting the importance of the packing of the bed as well as the size and shape of the grains. At a qualitative level, we can immediately see the effect of changing these properties however, in order to quantify their individual influence, we will address the main features of the post-impact dynamics.

4. Initial penetration

4.1. *Sphere motion*

During the very first moments after impact, the peak acceleration on the sphere occurs and may be as high as 50 g depending on the material in the bed and impact parameters as shown by Goldman & Umbahnowar (2008). In our experiments, we can directly track the motion of the sphere with high temporal resolution (50 000 or 70 000 f.p.s.) to show that within the first few milliseconds, the penetration rate is either virtually constant (e.g. glass beads with low packing fraction) or a rapid deceleration occurs (e.g. coarse sands with high packing fraction). This is shown by the example profiles in figure 5 where we plot the penetration depth versus time from

https://doi.org/10.1017/jfm.2012.141 Published online by Cambridge University Press

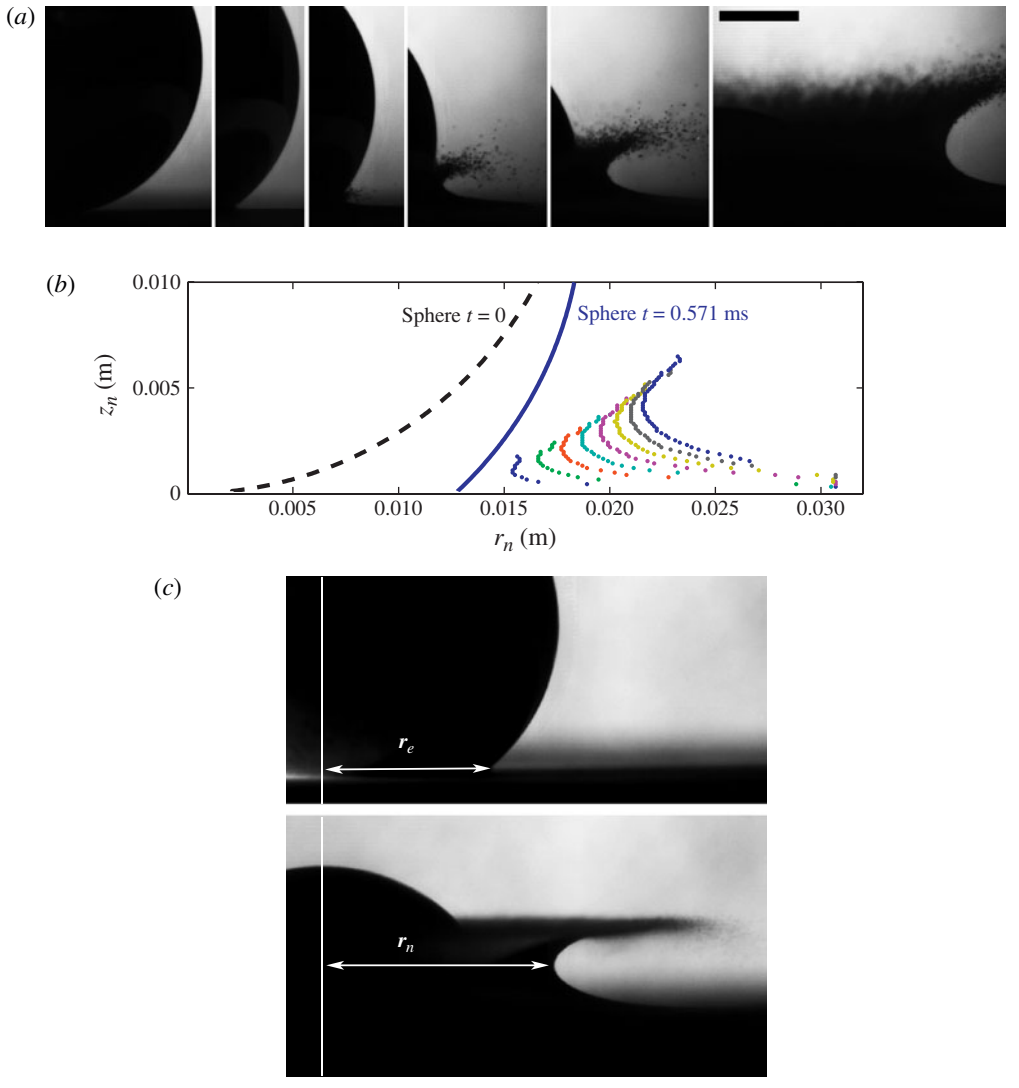


FIGURE 2. (*a*) Typical image sequence from a high-speed video clip taken at 70 000 f.p.s. showing the first stages of the granular ejecta following the impact of a $D_0 = 38$ mm steel sphere onto a bed of $d_b = 178$ μm grains with $V_0 = 9.05$ m s^{-1} ($Fr = 14.8$, $\phi = 0.58$ and $\varrho = 5.35$). Frames shown are taken at $t = 0$, 0.286, 0.571, 1.14, 1.71 and 3.14 ms from impact. The scale bar is 1 cm. (*b*) Locating the ejecta neck radius from the sequence in (*a*) after image analysis, where z_n is the height above the initial level and r_n is the horizontal distance from the axis of symmetry. Data sets show the granular edge at $t = 0.571$, 0.714, 0.857, 1.0, 1.14, 1.29, 1.43 and 1.57 ms from impact. The 'neck' radius is then defined to be the minimum value of r_n in each data set. (*c*) Images showing the emergence radius, $r_e = 12.3$ mm ($t_e = 220$ μs), and neck radius, $r_n = 23.7$ mm ($t = 1.45$ ms) for $D_0 = 38$ mm, $V_0 = 16$ m s^{-1} and $d_b = 31$ μm ($\varrho = 6.4$ and $Fr = 16.8$). The vertical line indicates the axis of symmetry.

impact for the 31 μm glass beads (*a,b*) and desert sand (*c,d*), respectively. Here, the penetration depth, H, is scaled with the sphere diameter, D_0, and the time is scaled with the characteristic time scale D_0/V_0.

https://doi.org/10.1017/jfm.2012.141 Published online by Cambridge University Press

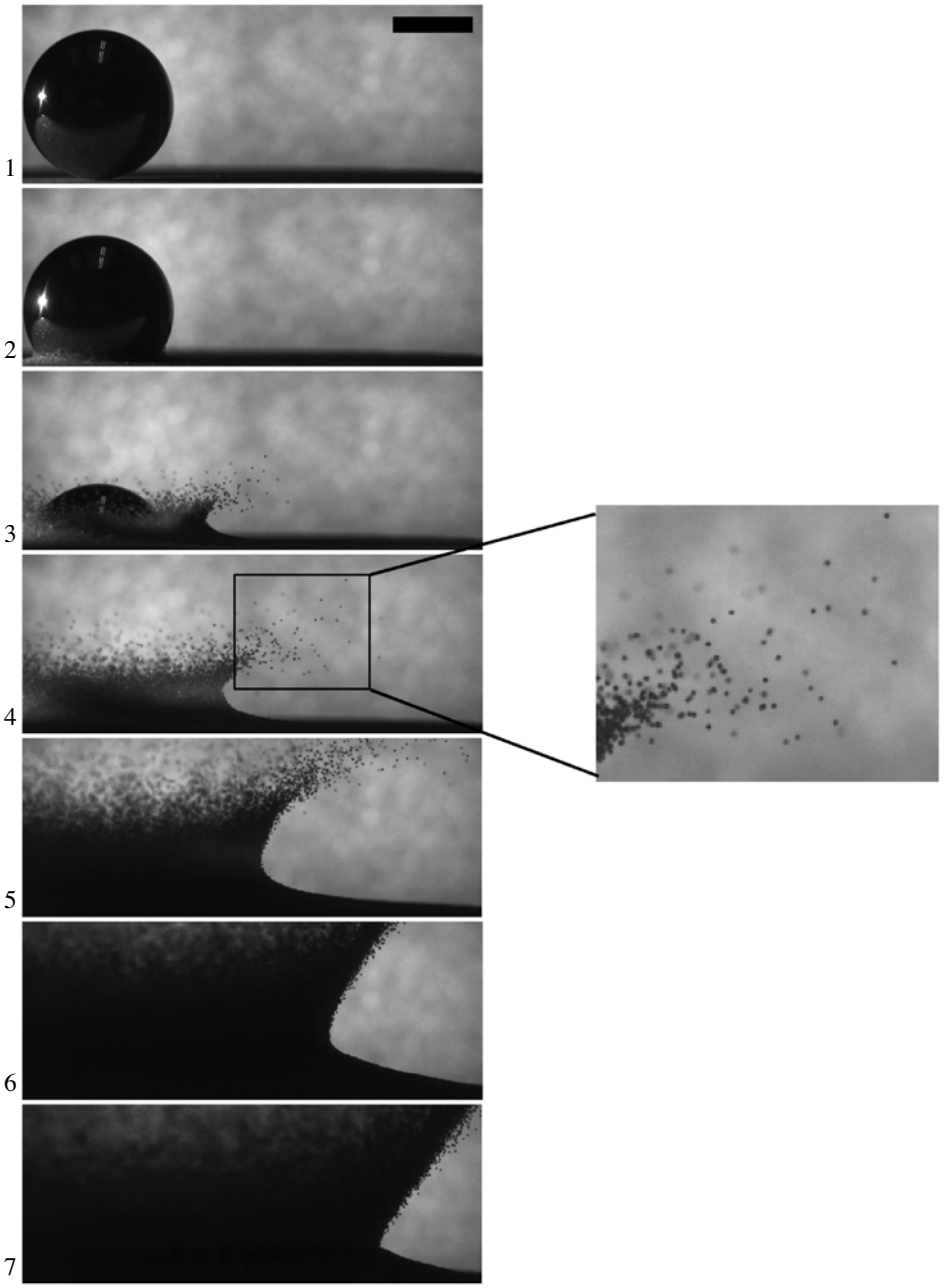


FIGURE 3. Images taken from a video sequence of the impact of a $D_0 = 38$ mm sphere onto a bed of 520 μm glass beads with $V_0 = 4.62$ m s^{-1} ($\phi = 0.59$, $\varrho = 5.3$, $Fr = 7.6$ and $\epsilon = 73$). The images are taken at times $t = 0$, 1.3, 5.3, 8.5, 19.1, 51.5 and 89.1 ms from impact. The scale bar is 2 cm long. The zoomed image shows the discrete grains which can be tracked through the field of view.

In each of these figures we plot data from multiple experimental conditions for the lowest (figure 5*a,c*) and the highest (figure 5*b,d*) ϕ obtained. The collapsed profiles

https://doi.org/10.1017/jfm.2012.141 Published online by Cambridge University Press

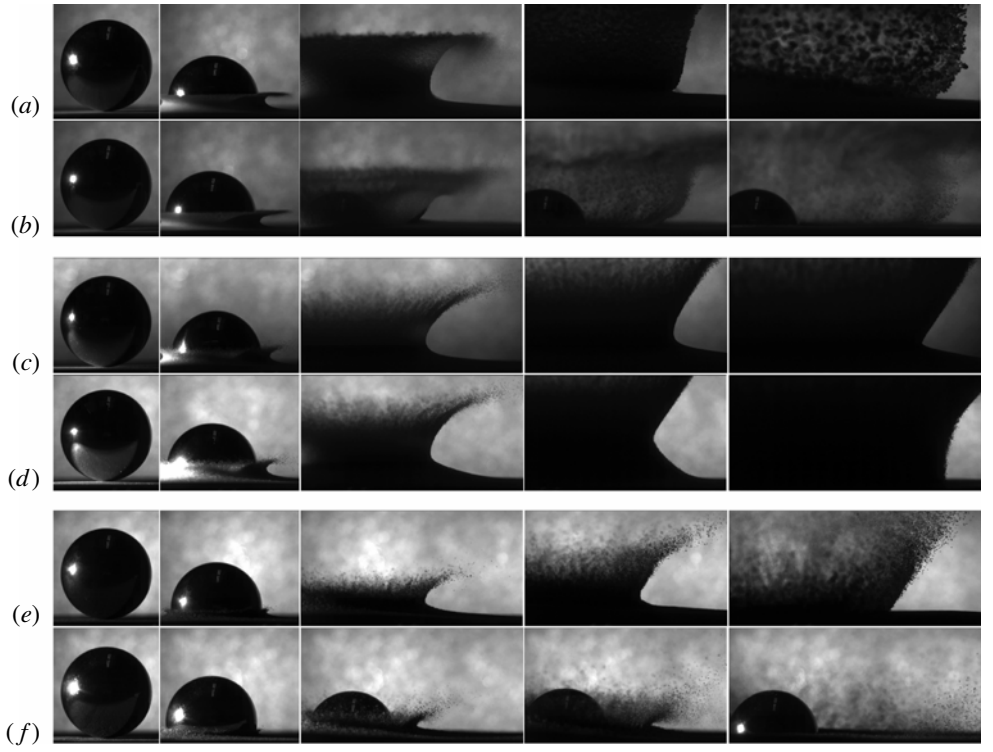


FIGURE 4. Image sequences from high-speed video clips taken at 30 000 f.p.s.: (*a*) glass beads $d_b = 31$ μm, $\phi = 0.49$; (*b*) glass beads $d_b = 31$ μm, $\phi = 0.61$; (*c*) glass beads $d_b = 178$ μm, $\phi = 0.59$; (*d*) glass beads $d_b = 178$ μm, $\phi = 0.64$; (*e*) desert sand $d_b = 301$ μm, $\phi = 0.59$; (*f*) desert sand $d_b = 301$ μm, $\phi = 0.68$. Images in each row are taken at $t = 3.3$, 13.3, 30 and 80 ms from impact. In each sequence $V_0 = 4.63$ m s^{-1}, $D_0 = 38$ mm yielding $Fr = 7.6$ (with $\varrho = 6.4$, 5.1, 5.3, 4.9, 5.3 and 4.6; $\epsilon = 806$, 806, 140, 140, 83 and 83). Note that the sphere has come to rest in the final images of sequences (*b–f*).

in figure 5(*a*) suggest that for $H/D_0 \geqslant -0.5$, the sphere penetrates without significant deceleration. In contrast, for the higher packing fraction shown in figure 5(*b*), we can already see some significant deceleration by the time $H/D_0 = -0.5$. The data points become immeasurable after $H/D_0 \approx -0.7$ as the ejecta obscures the camera view. One notable feature in figure 5(*b*) for the fine grains ($d_b = 31$ μm) is that the data for $D_0 = 50$ mm becomes distinct from $D_0 = 25$ and 38 mm, which may be an indication of the onset of confinement effects at this packing fraction (Goldman & Umbahnowar 2008; Umbanhowar & Goldman 2010).

The deceleration of the sphere becomes more pronounced when impacting onto the coarse sands, as shown by the profiles in figure 5(*c,d*). There is a small deviation from the constant-velocity trajectory for the low packing fractions in figure 5(*c*) which is greatly magnified as the packing fraction is increased in figure 5(*d*). The strongest deceleration observed herein is for the beach sand with $\phi = 0.67$ and $D_0 = 50$ mm. Here, we can see that the sphere's motion has been almost completely arrested by $T = 1$ and has penetrated less than one radius into the sand surface level. We can attribute this strong deceleration to both size and shape distribution, since the beach sand has the broadest size distribution (absolute and relative) and the lowest circularity

https://doi.org/10.1017/jfm.2012.141 Published online by Cambridge University Press

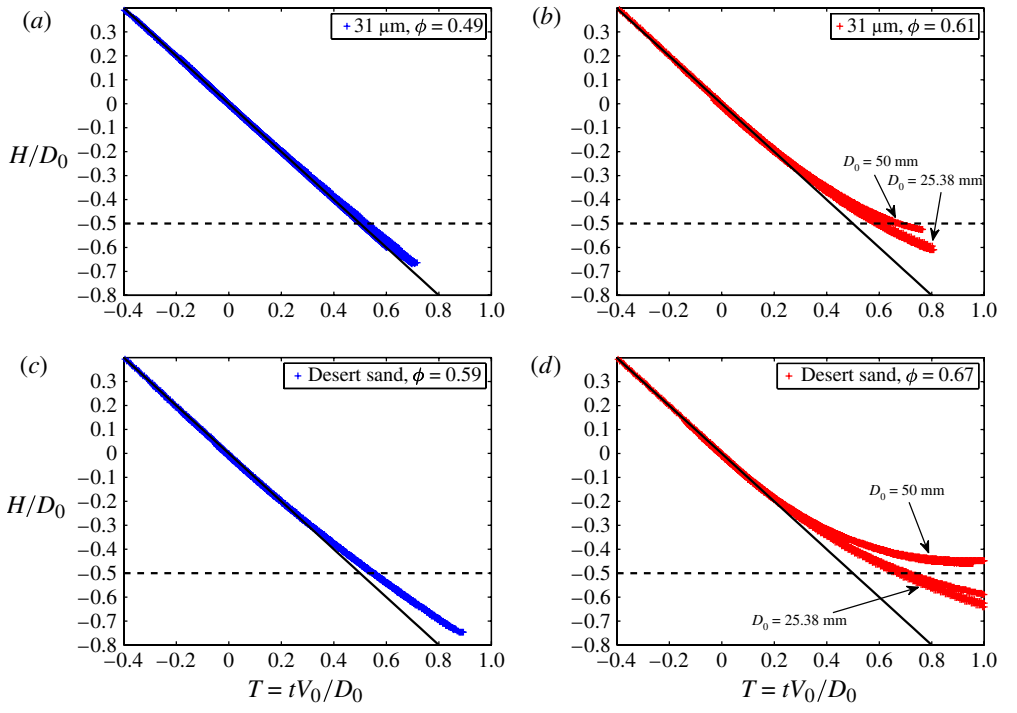


FIGURE 5. Normalized penetration depth H/D_0 versus normalized time $T = tV_0/D_0$ for multiple experimental conditions; (*a*) glass beads $d_b = 31$ μm, $\phi = 0.49$, $D_0 = 25$, 38 and 50 mm, $V_0 = 2.6$, 4.77 and 9.81 m s^{-1}. (*b*) Glass beads $d_b = 31$ μm, $\phi = 0.61$, $D_0 = 25$, 38 and 50 mm, $V_0 = 4.63$ m s^{-1}. (*c*) Desert sand, $\phi = 0.59$, $D_0 = 25$, 38 and 50 mm, $V_0 = 4.63$ m s^{-1}. (*d*) Desert sand, $\phi = 0.67$, $D_0 = 25$, 38 and 50 mm, $V_0 = 4.63$ m s^{-1}. The solid lines represent the trajectory under a constant velocity whilst the horizontal dashed line represents a penetration depth of one sphere radius.

measurement. These two properties play a key role determining the amount of particle interlocking and resistance to shear (Housen & Holsapple 2011) and may be related to the bearing capacity for soils (Stephensen 2000).

4.2. *Emergence radius*

The first grains are ejected from the bed surface within the first few milliseconds from impact and we accurately identify this first ejection with close-up imaging, to extract the 'emergence radius' and associated 'emergence time'.

Formally, we define the emergence radius as the horizontal distance from the centre of the impact site to the radial location at which the first grains (or sheet) emerge and denote this as r_e and the corresponding time to reach r_e taken from impact is denoted t_e. Data for r_e and t_e are essential for analysis of the ejecta evolution since we need a reference time and location for the start of the ejecta. Clearly, $t = 0$ is not particularly useful as a reference for the ejecta evolution because there is no ejecta for $0 \leqslant t < t_e$.

As such, for $t \leqslant t_e$, if one assumes the velocity of the sphere to be approximately constant, i.e. $V_s(t) \sim V_0$, then one can write $r_t = \sqrt{V_0 t_e (D_0 - V_0 t_e)}$ for the radial position where the sphere intersects the bed surface at time t_e. In figure 6(*a*) we can see that r_t is consistently smaller than the actual emergence radius r_e by a factor of approximately 1.15 (red dashed line in figure 6*a*). This means there is a small amount

https://doi.org/10.1017/jfm.2012.141 Published online by Cambridge University Press

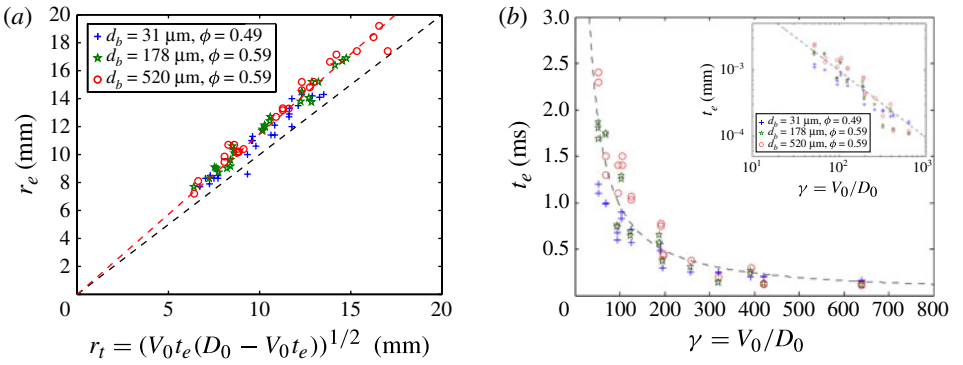


FIGURE 6. (*a*) Emergence radius r_e at time t_e when the grains first emerge plotted against the predicted radius $r_t = \sqrt{V_0 t_e (D_0 - V_0 t_e)}$. Data for fixed ϕ, $D_0 = 25$, 38 and 50 mm and $2.6 \leqslant V_0 \leqslant 16$ m s^{-1}. (*b*) Emergence time t_e versus impact shear rate $\gamma = V_0/D_0$, the dashed line indicates a fit to the data with $t_e \propto \gamma^{-1}$.

of granular material between the sphere and the emergence radius which is expected since granular material can undergo local compaction before reaching a critical state (Umbanhowar & Goldman 2010).

In figure 6(*b*), we observe that the emergence time for the grains ranges between 110 μs–2.5 ms and is inversely related to the impact shear rate (see also § 8.1), i.e. $t_e \propto (V_0/D_0)^{-1}$, with data collapsing onto a single curve indicating that t_e is essentially independent of the size of the grains.

We note that the shortest emergence time, $t_{e,min} = 110$ μs is considerably longer than that for the liquid ejecta emerging from the impact site of a sphere onto water which typically occurs within 10 μs from impact (Thoroddsen *et al.* 2004). This is certainly due to the fact that the granular beds undergo a local compaction during impact compared with the incompressible water case.

Figure 7(*a–d*) show dimensionless forms of both the emergence radius, $2r_e/D_0$, and emergence time, $t_e V_0/D_0$, versus the impact Froude number and size ratio, respectively, for a single packing fraction for each of the glass beads. Figure 7(*a,b*) show that the non-dimensional radius and time are virtually independent of the impact Froude number, indicating that D_0 and D_0/V_0 are indeed the correct scalings for the emergence radius and emergence time respectively. In figure 7(*c,d*) we note that both the emergence radius and time both exhibit a weak dependence on the size ratio, $\epsilon = D_0/d_b$. Thus, at first order, it appears that both the emergence radius and time are independent of Fr and ϵ

In a similar fashion, figure 8(*a–d*) show equivalent data for the non-dimensional emergence radius and time for a fixed impact velocity, versus both packing fraction (*a,b*) and size ratio (*c,d*). From all of the figures, we can immediately see that there is a clear distinction between the two types of material, namely the glass beads, with a nearly spherical shape and narrow size distribution, where the normalized emergence radius $2r_e/D_0 \leqslant 0.8$ and the sands, with highly non-spherical shape and broad size distribution, where $2r_e/D_0 \geqslant 0.8$. There is also a clear distinction between the emergence times for the sands and glass beads with the sands exhibiting a delayed response with higher values of t_e and a broader range with $1 \leqslant t_e \leqslant 2.5$ ms ($t_e V_0/D_0 > 0.15$), whereas for the glass beads $0.5 \leqslant t_e \leqslant 1$ ms ($t_e V_0/D_0 < 0.15$).

https://doi.org/10.1017/jfm.2012.141 Published online by Cambridge University Press

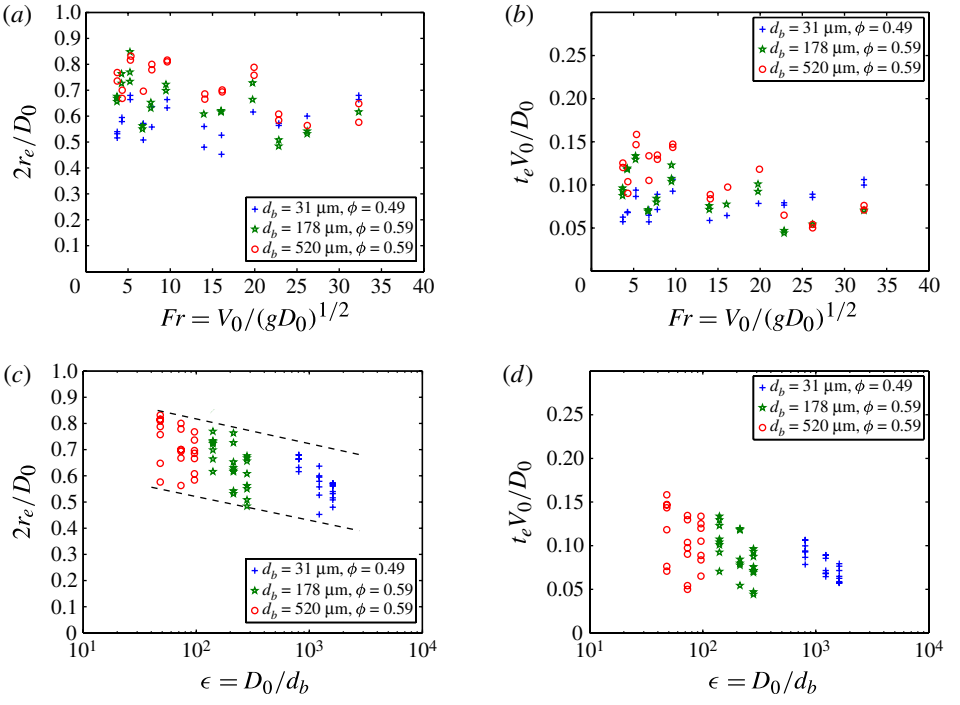


FIGURE 7. (*a*) Normalized emergence radius $2r_e/D_0$ and (*b*) normalized emergence time t_eV_0/D_0, both versus impact Froude number, $Fr = V_0/(gD_0)^{1/2}$, for glass beads at fixed packing fractions (see legends). (*c,d*) The same data plotted against the size ratio, $\epsilon = D_0/d_b$. (Here $D_0 = 25$, 38 and 50 mm and $V_0 = 2.6$–16 m s^{-1}.)

Figure 8(*a,b*) indicate that the packing fraction has virtually no influence on the emergence radius and time for both the glass beads and the sands. Thus, at first order, it appears that both the emergence radius and time are independent of Fr, ϵ and ϕ.

However, from figure 8(*c,d*), there is a slightly stronger dependence on ϵ for the coarse sands, which implies that size distribution and shape may be important. This finding implies that the emergence radius and time could, in principle, be used as an alternative measure of particle 'interlocking' (Housen & Holsapple 2011) of a granular material since it is virtually independent of the initial solids packing fraction during impact. The fact that the sands are largely non-spherical and have a broader size distribution may allow for a larger compaction or local restructuring of the voids compared with the glass beads during the moment of impact thus leading to higher emergence times and radii. Although we cannot measure any dynamic change in the local packing, in previous studies a local change in packing fraction, $\Delta\phi$, of up to 6 % was found during impact (Royer *et al.* 2007).

From figure 8(*b,d*), we find mean values for the normalized emergence time, $t_eV_0/D_0 \approx 0.1$ for the glass beads and $t_eV_0/D_0 \approx 0.22$ for the sands. Re-arranging for t_e and substituting into $r_e \approx 1.15r_t$, we find that $2r_e/D_0 \approx 0.69$ for the glass beads and $2r_e/D_0 \approx 0.95$ for the sands, which are close to the experimental values (figure 8*a,c*). Thus, the emergence radius is controlled by the emergence time and sphere diameter, i.e. $r_e = f(t_e, D_0)$ and independent of Fr, ϕ and ϵ.

https://doi.org/10.1017/jfm.2012.141 Published online by Cambridge University Press

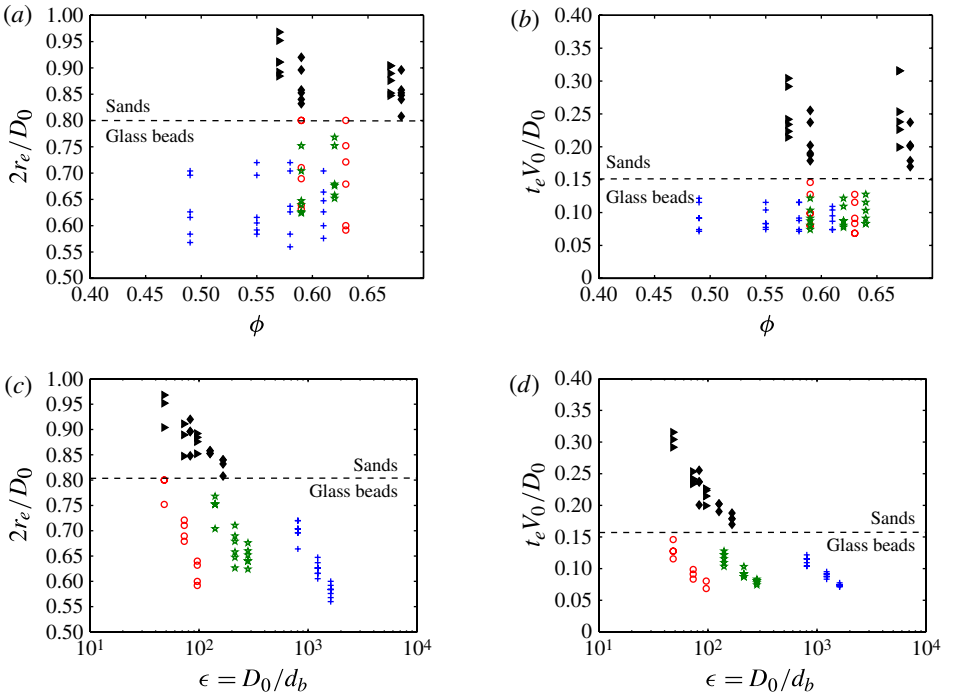


FIGURE 8. (*a*) Normalized emergence radius $2r_e/D_0$ and (*b*) normalized emergence time t_eV_0/D_0, both versus initial packing fraction, ϕ, for both glass beads and sands at fixed impact velocity $V_0 = 4.5$ m s^{-1}. (*c,d*) The same data plotted against the size ratio, $\epsilon = D_0/d_b$. (Here $D_0 = 25$, 38 and 50 mm.) Symbols indicate different materials as follows: (+) glass beads, $d_b = 31$ μm; (⋆) glass beads $d_b = 178$ μm; (○) glass beads, $d_b = 520$ μm; (▷) beach sand, $d_b = 524$ μm; (◇) desert sand, $d_b = 310$ μm.

5. Grain ejection for large grains

Previous studies in ejecta velocity distributions involving impact velocities $V_0 = O(1)$ km s^{-1} have derived the effective 'main-stage' ejecta velocities and angles (measured from the horizontal plane of the bed surface) using mass collected in bins at set distances from the impact site (e.g. Hartmann 1985; O'keefe & Ahrens 1985; Michikami *et al.* 2007) or the ejecta velocity was a fitting parameter in the analysis (Deboeuf *et al.* 2009). In addition, particle tracking velocimetry (PTV) has been applied to particles residing on the edge of the fully developed ejecta in order to deduce the velocity once the ejecta curtain has formed (e.g. Hermalyn & Schultz 2010, 2011), however these measurements were made with somewhat lower temporal resolution than in our experiments. For the main stage ejecta, velocities are typically scaled with the characteristic velocity $\sqrt{gR_c}$ where R_c is the final crater radius and time is scaled with $\sqrt{R_c/g}$ under the assumption of point-source ejection (Hermalyn & Schultz 2011; Housen & Holsapple 2011).

In this section, however, we are concerned with the early stage flow, i.e. the velocities of the very first-ejected individual grains. This is achieved through the direct tracking of individual grains over several frames which yields the actual ejection velocity and angle (assuming a linear trajectory over the time interval for the tracking, which was checked and verified for each video clip). In this early stage

https://doi.org/10.1017/jfm.2012.141 Published online by Cambridge University Press

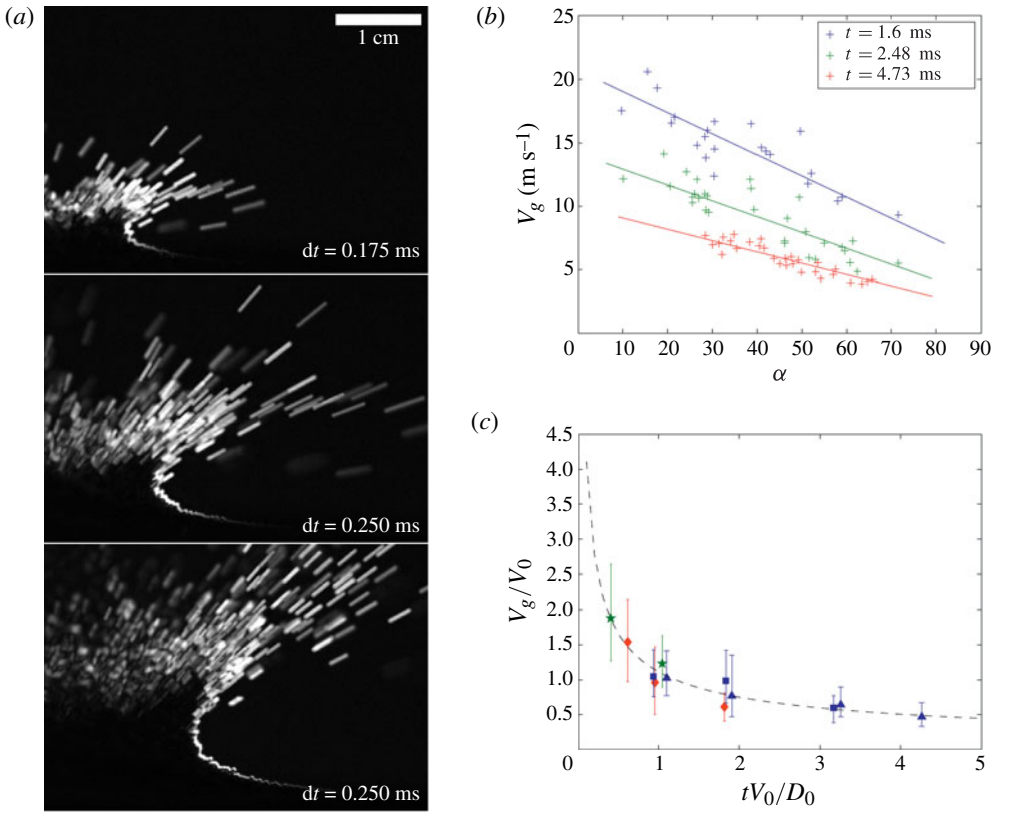


FIGURE 9. (*a*) Images showing particle streaks over 7-frame (dt = 175 µs) and 10-frame (dt = 250 µs) intervals for $d_b = 520$ µm, $V_0 = 9.6$ m s^{-1}, $D_0 = 25$ mm, $\phi = 0.59$ at times $t = 1.6$, 2.48 and 4.73 ms from impact. Here $Fr = 19.4$, $\varrho = 5.3$ and $\epsilon = 48$. (*b*) Corresponding plots of velocity V_g versus angle α from horizontal extracted from the images. (*c*) Normalized ejection velocity V_g/V_0 versus normalized time tV_0/D_0 from impact for $D_0 = 25$ mm $V_0 = 4.5$ m s^{-1} (blue), 9.8 m s^{-1} (red) and 16 m s^{-1} (green), with ($\star$, $\diamond$, $\triangle$) $\phi = 0.59$ and ($\square$) $\phi = 0.63$. Data points indicate the mean whilst the error bars incorporate the maximum and minimum velocity measured.

flow, i.e. before the main ejecta curtain has formed, it is expected that the ejection velocities decrease with time from impact with the characteristic time scale being D_0/V_0 (Holsapple 1993) and the ejection angles increase since the flow approaches the main-stage ejecta flow (Hermalyn & Schultz 2010) where $\alpha \sim 45°$ and the bulk of the ejected grains are confined to the ejecta 'curtain'. As such the range of ejection angles and velocities are both expected to decrease with time from impact. Here, we provide quantitative evidence of this in terms of instantaneous velocities by analysing streakline images.

5.1. *Instantaneous grain velocities and influence of packing fraction*

Figure 9(*a*) shows streak images of the ejected particles from a bed of $d_b = 520$ µm grains following the impact of a $D_0 = 25$ mm sphere at $V_0 = 9.6$ m s^{-1}. The images have been inverted and processed using Davis software (LaVision GmbH). The corresponding plot of ejection velocity, V_g, versus ejection angle, α, is shown in

https://doi.org/10.1017/jfm.2012.141 Published online by Cambridge University Press

figure 9(*b*) along with data from other trials. Here we can see that not only do the velocities decrease with time from impact, but that at each instance ($t = 1.6$, 2.48 and 4.73 ms), the velocity decreases as the ejection angle increases. Furthermore, we can also see that the range of velocities and angles also narrows as time progresses. This is a clear indication that the flow is converging towards the 'main-stage ejecta flow'.

In figure 9(*c*) we plot the ejection velocity versus time from impact for a range of data sets each with a variety of impact velocities and initial packing fractions. Here, the data points indicate the mean whilst the error bars incorporate maximum and minimum values measured. In the early stage flow, we scale velocities with the impact velocity, V_0, and time with the time scale, D_0/V_0. Using these scalings, we can assess the dependence of the ejecta evolution on both the granular material and packing fraction. Surprisingly, there does not appear to be any marked difference between the data sets which all appear to exhibit the same trend whereby the range of velocities and the magnitude of the velocities both decrease as time from impact increases. From this data, based on the convergence of the error bars, we conclude that the main-stage flow is reached at $tV_0/D_0 \sim 5$ for the 520 μm beads, i.e. that the main-stage flow or 'excavation flow' begins once the sphere has penetrated to a depth $H \geqslant 5D_0$ into the bed.

Equivalent data for the 178 μm glass beads and for the two coarse sands are shown in figure 10(*a,b*) respectively. In figure 10(*a*), we observe a similar behaviour to that in figure 9(*c*) only that the transition to 'main-stage ejecta flow' appears to occur slightly earlier, with $tV_0/D_0 \sim 4$. For the sands, however, we observe a qualitatively different behaviour with the first ejected grains occurring at much later times ($tV_0/D_0 > 1$) than for the glass beads where grains emerge at times as small as $tV_0/D_0 \sim 0.1$ (see § 5.2). In figure 10(*b*) we see a small decrease in ejection velocity with time but again, no distinct trend between the different packing fractions (different symbols) used. As such, it appears that the initial packing fraction has a negligible effect on the first ejected grains. That is to say the early stage flow is rather insensitive to the initial packing fraction. We do, however, observe significant differences between the ejection velocities for the glass beads and the sands which indicates that, as for the initial emergence radius, the particle shape and size distribution play dominant roles. This is natural as the shape and size distribution are the parameters governing the amount of particle 'interlocking' and thus the resistance to shear deformation.

5.2. *Scaling the early stage velocities for glass beads*

Figure 11(*a*) plots the normalized grain ejection velocity V_g/V_0 against ejection angle α for the 520 μm glass beads over a range of impact velocities and sphere sizes showing that the ejection velocity increases with both increasing sphere size and impact velocity. Furthermore, each data set also shows that as the ejection angle increases, the ejection velocity decreases. That is to say the fastest grains are generally ejected at the lowest angles. Figure 11(*b*) plots the ejection angle, α, for the same data in (*a*) against normalized time, tV_0/D_0, showing that α generally increases with time for $tV_0/D_0 \leqslant 0.5$. There is considerable scatter in the data with a large range of angles for any given time, which may be expected as there will be significant particle–particle collisions close to the ejection point. The solid red line in figure 11(*b*) represents $\alpha = \cos^{-1}(1 - 2tV_0/D_0)$, which is the angle of the tangent of the sphere surface at the geometric intersection point $r_t = \sqrt{V_0 t(D_0 - V_0 t)}$ of the sphere with the initial granular surface. A similar geometric argument was also made by Thoroddsen *et al.* (2011) for the ejecta sheet in liquid drop impacts. As seen in the plot, the half-angle $\alpha = \cos^{-1}(1 - 2tV_0/D_0)/2$ shown by the green line provides a better description of

https://doi.org/10.1017/jfm.2012.141 Published online by Cambridge University Press

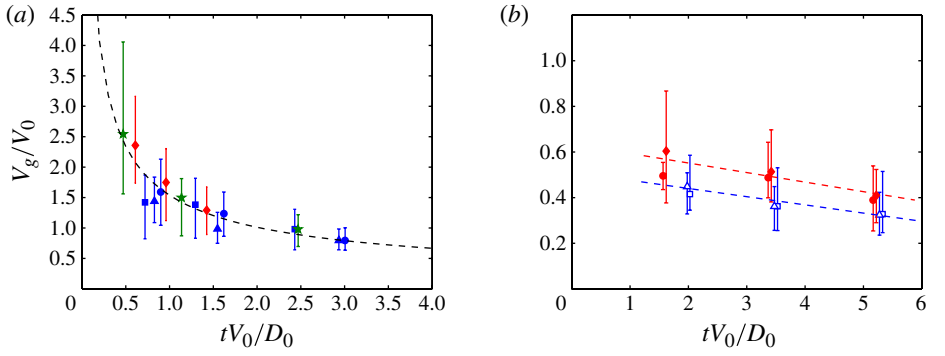


FIGURE 10. Normalized ejection velocity V_g/V_0 versus normalized time tV_0/D_0 for (*a*) $d_b = 178$ μm, $D_0 = 25$ mm, $V_0 = 4.5$ m s^{-1} (blue), 9.8 m s^{-1} (red) and 16 m s^{-1} (green), with (○, △, ⋆) $\phi = 0.59$, (◇) $\phi = 0.62$ and (□) $\phi = 0.64$. (*b*) Desert sand (red) and beach sand (blue), $D_0 = 25$ mm, $V_0 = 4.5$ m s^{-1}, with (□) $\phi = 0.67$, (△) $\phi = 0.57$, (○) $\phi = 0.68$ and (◇) $\phi = 0.59$.

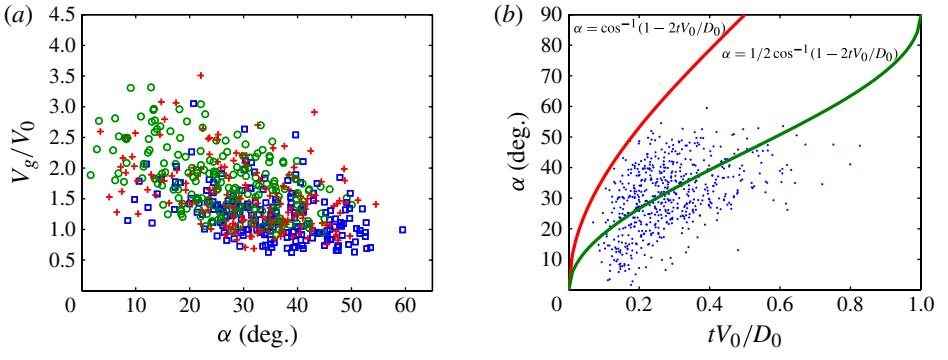


FIGURE 11. (*a*) Individual grain ejection velocities (normalized by impact velocity) V_g/V_0 versus ejection angle α for $d_b = 520$ μm glass beads ($\phi = 0.59$, $\varrho = 5.3$, $Fr = 3.8$–32) with impacting sphere sizes (□) $D_0 = 25$ mm, (+) 38 mm and (○) 50 mm. (*b*) Ejection angles α from (*a*) versus normalized time tV_0/D_0. The solid lines represent the angle (red) and half-angle (green) of the tangent of the sphere at the intersection point (see the text).

the mean ejection angle in time. At later times, however, the ejection angle reaches a constant value of approximately 45–50°, which was also found by Hermalyn & Schultz (2011) for hypervelocity impacts.

The fastest grains also emerge at the earliest times (close to the emergence time, t_e), as shown in figure 12(*a*) where all data points from figure 11 are replotted as ejection velocity versus ejection time. Here, the ejection time, t, is the time measured from impact and has been normalized by D_0/V_0. From this plot, it is clear that all data collapses onto a single master curve. For the realizations analysed herein, we find the fastest grains with $V_g/V_0 = 3$–3.5 emerging at the earliest times with $T = tV_0/D_0 < 0.1$. The slowest grains, i.e. $V_g/V_0 \sim 0.7$, ejected at higher angles, are those ejected at latter times with $T > 0.5$.

https://doi.org/10.1017/jfm.2012.141 Published online by Cambridge University Press

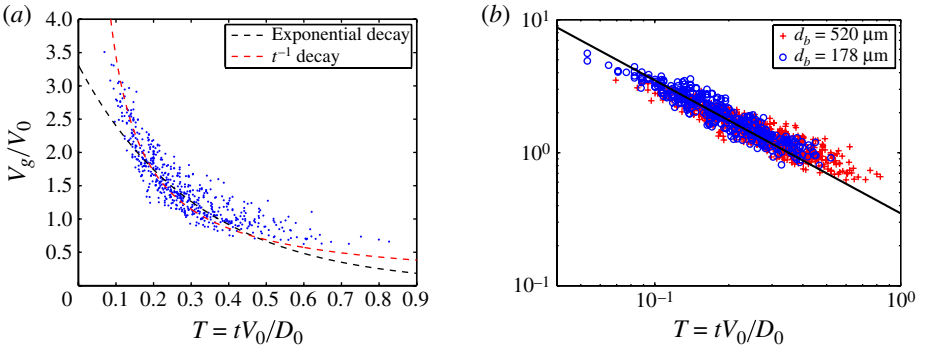


FIGURE 12. (*a*) Ejection velocity (normalized by sphere impact velocity) V_g/V_0 versus ejection time (normalized by characteristic time scale) TtV_0/D_0 for $d_b = 520$ μm glass beads with $\phi = 0.59$ ($\varrho = 5.3$). All data points from figure 11 are included. Dashed lines indicate fits to the data showing exponential and inverse decay of velocity with time. (*b*) Normalized ejection velocities versus normalized time scale, $T = tV_0/D_0$. All data for both 178 and 520 μm beads with $T < 1$ are shown.

Similar trends of velocity versus ejection angle are also observed for the $d_b = 178$ μm glass beads. However, we note that the highest values of V_g/V_0 are generally higher than for the 520 μm beads where the fastest grains ($V_g/V_0 > 3.5$) emerge at the earliest times ($T = tV_0/D_0 < 0.1$) whilst at later times $V_g/V_0 \to 1$ for $tV_0/D_0 > 0.3$.

For both the 178 and 520 μm glass beads, we also observe that the ejection velocity of individual grains decays with time from impact. For example, in figure 12(*a*) we plot fits to the data for both exponential and inverse decay of velocity in time, showing that the inverse time decay provides a better fit over the range of velocities measured here with $V_g/V_0 \approx kT^{-1}$ where k is a constant which takes the value 0.34 for $d_b = 178$ μm and 0.35 for $d_b = 520$ μm. All data for both the 178 and 520 μm glass beads are shown in figure 12(*b*) showing that the two data sets collapse when scaled as above. This finding could be useful in improving models of grain ejection such as that presented by Deboeuf *et al.* (2009).

For hypervelocity impacts with $V_0 = O(1\ \mathrm{km\ s^{-1}})$, Hermalyn & Schultz (2011) scale the early time ejecta velocities with the impact velocity whilst the temporal scaling takes the following form

$$\tau = \frac{tV_0}{D_0}\left(\frac{\rho_b^{\nu} c^{\mu}}{\rho_0^{\nu} V_0^{\mu}}\right) \equiv T\varrho^{-\nu}\left(\frac{c}{V_0}\right)^{\mu}, \tag{5.1}$$

where $c = 180\ \mathrm{m\ s^{-1}}$ and the exponents $\nu = 1/3$ and $\mu = 2/3$ are found to best fit experimental data. Under this modified time scale, we find data for both grain sizes $d_b = 178$ and 520 μm do not collapse as well as for the simple time scale $T = tV_0/D_0$ (as shown in figure 12*b*). Note that our simple scaling implies that $V_g \sim D_0/t$ whilst that of Hermalyn and Schultz implies $V_g \sim V_0^{-1/3} D_0/t$, indicating that their modified scaling may not be applicable for low-velocity impacts such as in our experiments.

5.3. *Impactor kinetic energy*

The influence of both the sphere diameter and impact velocity on the grain ejection velocities can be summarized in terms of the impact kinetic energy; as the impact

https://doi.org/10.1017/jfm.2012.141 Published online by Cambridge University Press

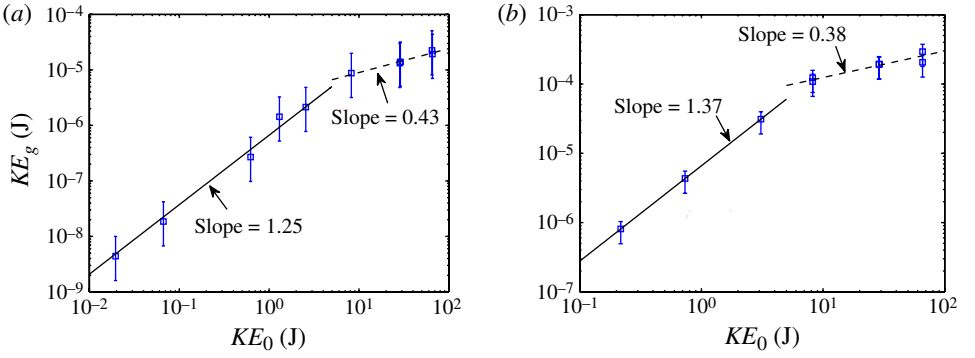


FIGURE 13. Grain kinetic energy KE_g versus impact kinetic energy KE_0 for (*a*) $d_b = 178$ μm ($\epsilon \in (112, 280)$, $\varrho = 5.3$) and (*b*) $d_b = 520$ μm ($\epsilon \in (38, 96)$, $\varrho = 5.3$). The data points indicate the mean grain energy for the data set (with $tV_0/D_0 \leqslant 0.5$) and the vertical bars encompass the minimum and maximum, respectively. The solid and dashed lines indicate power-law best fits to the data with exponents of (*a*) 1.25 and 0.43, (*b*) 1.37 and 0.38 respectively.

Study	$\epsilon = D_0/d_b$	KE_0 (Joules)	Scaling
Deboeuf *et al.* $d_b = 400$ μm	25–50	5×10^{-3}–2×10^{-1}	$V_g \propto KE_0^{0.18}$
Colwell *et al.* $d_b = 75$–500 μm	20–190	10^{-5}–10^{-2}	$V_g \propto KE_0^{0.5}$
Present work $d_b = 178$ μm	112–280	10^{-2}–5	$V_g \propto KE_0^{0.62}$
Present work $d_b = 178$ μm	112–280	5–10^2	$V_g \propto KE_0^{0.21}$
Present work $d_b = 520$ μm	38–96	10^{-2}–5	$V_g \propto KE_0^{0.67}$
Present work $d_b = 520$ μm	38–96	5–10^2	$V_g \propto KE_0^{0.19}$

TABLE 3. Summary of scalings of grain ejection velocities with impact kinetic energy from Deboeuf *et al.* (2009), Colwell *et al.* (2008) and data from figure 13 herein.

kinetic energy increases, the initial grain ejection energy increases. This is evident in figure 13 where we plot the mean grain kinetic energy, KE_g, as a function of impact kinetic energy, KE_0. Here, we see that the data for both grain sizes exhibit similar trends with two discrete regions becoming apparent; for low impact energies ($KE_0 \leqslant 5$), $KE_g \propto KE_0^{1.25}$ for $d_b = 178$ μm and $KE_g \propto KE_0^{1.37}$ for $d_b = 520$ μm whilst for $KE_0 > 5$, $KE_g \propto KE_0^{0.43}$ for $d_b = 178$ μm and $KE_g \propto KE_0^{0.38}$ for $d_b = 520$ μm.

These scalings show a much more significant influence of KE_0 on KE_g (and, hence, V_g) than previously observed by Deboeuf *et al.* (2009) where the scaling $KE_g \propto KE_0^{0.37}$ was found. Colwell *et al.* (2008) found that the average ejecta velocity scales as $V_{ej} \propto KE_0^{1/2}$, thus implying $KE_g \propto KE_0$ for low-impact-speed experiments in low gravity with both silica and regolith simulant particles.

We do note, however, the differences in the experimental set-ups between our experiments and those of Deboeuf *et al.* (2009) and also that their velocities were extracted through fitting, not direct tracking at early times. Also, of interest is the range of impactor-to-grain size ratios, ϵ, used. A summary of these parameter ranges and deduced scalings is given in table 3. When considering the scalings, one should

https://doi.org/10.1017/jfm.2012.141 Published online by Cambridge University Press

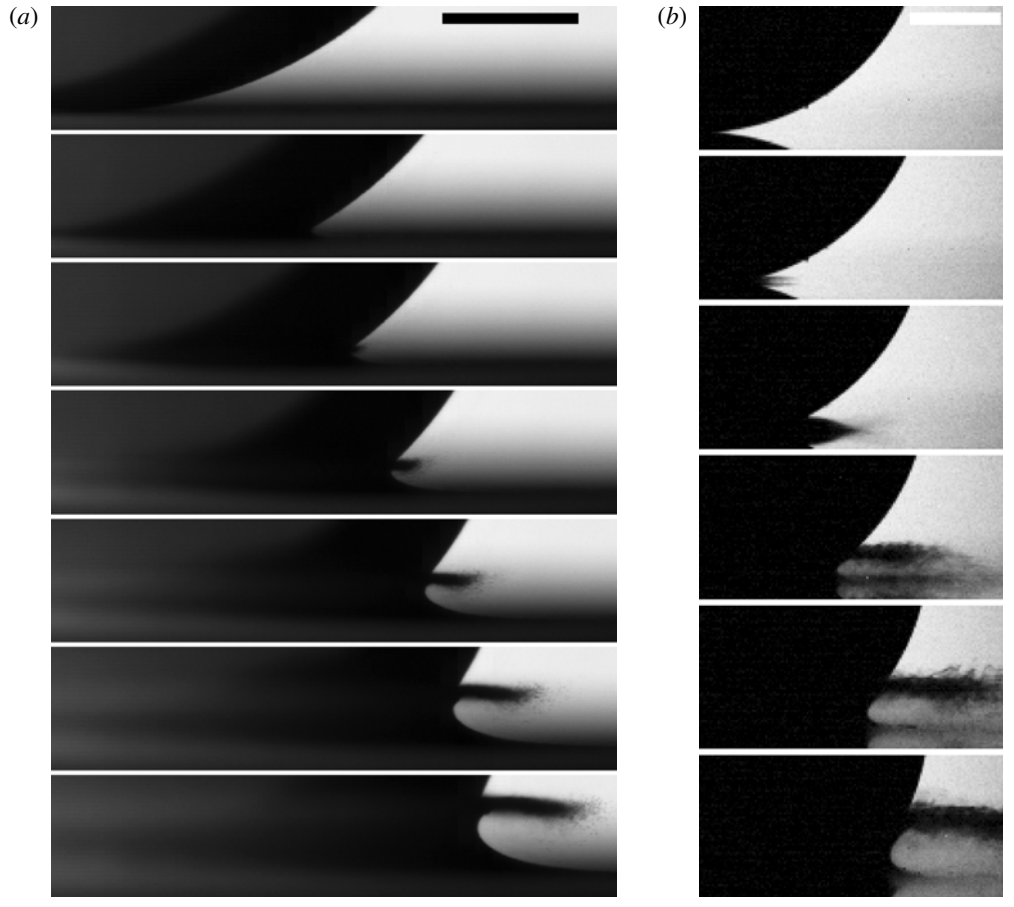


FIGURE 14. Frames from high-speed video sequences taken at 100 000 f.p.s. showing (*a*) the emergence of the sheet for $D_0 = 0.05$ m, $V_0 = 2.61$ m s^{-1} ($Fr = 3.7$, $\epsilon = 1600$, $\varrho = 6.4$ and $\phi = 0.49$) at $t = 0$, 1.07, 1.47, 1.97, 2.47, 2.97 and 3.47 ms from impact (see also supplementary video 2). The sheet velocity in (*a*) over the first few frames is $V_s \sim 7.7$ m s^{-1}. (*b*) High-speed ejecta for impact onto water ($Fr = 9.79$, $\varrho = 7.8$ taken at $t = 0$, 20, 70, 170, 270 and 370 μs from first contact showing the fine ejecta (frame 2) that hits the surface (frame 3) before the main ejecta (frame 4) evolves (see also supplementary video 3). The scale bars are 10 and 5 mm, respectively.

bear in mind the limitations of the experiments in the respective studies and the fact that in the present work, the scalings were deduced for the first ejected grains. Also, as shown in the table 3, in Deboeuf *et al.* (2009) $D_0/d_b \sim 25$–50, while in Colwell *et al.* (2008) $D_0/d_b \sim 20$–190 and in figure 13 herein $D_0/d_b \sim 50$–280 which indicates that different scalings may hold for different ratios, the effect of grain size and shape distribution notwithstanding.

6. Sheet dynamics for fine grains

6.1. *Sheet velocity*

For the finest grains used in these experiments, i.e. $d_b = 31$ μm, the first grains ejected from the bed form a sheet-like structure, such as that shown in figure 14(*a*) which

https://doi.org/10.1017/jfm.2012.141 Published online by Cambridge University Press

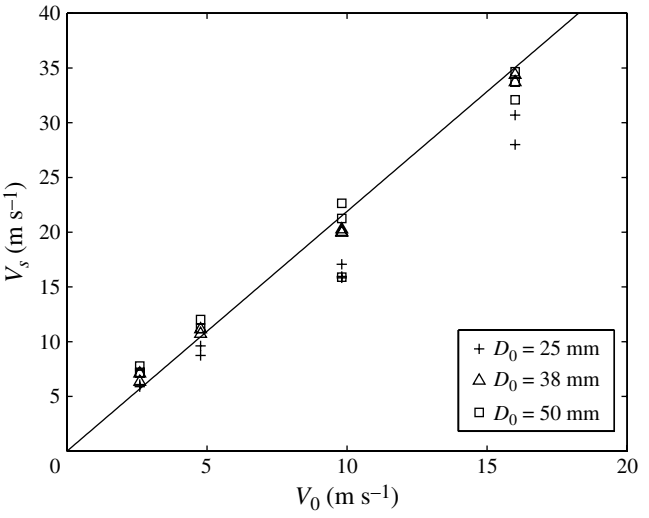


FIGURE 15. Sheet velocities V_s versus impact velocity V_0 from experiments performed at four different release heights with constant initial packing fraction, $\phi = 0.49$. The solid line represents the ratio $V_s/V_0 = 2.2$.

is similar in appearance to that seen for solid-body impacts onto water (Thoroddsen *et al.* 2004). The tip of the sheet is blurred due to separation of individual grains from the sheet but is clearly approaching a more fluid-like structure than for the larger grain sizes (see figures 1*a*, 1*b*, 2*a*, 3 and 4*c–f*). In figure 14(*a*), the sheet emerges at $t_e \sim 1.07$ ms from impact with an almost horizontal trajectory with an average sheet velocity (calculated from the first ∼20 frames after t_e) $V_s = 7.7$ m s^{-1} which gives the ratio $V_s/V_0 \sim 3$ for this particular realization. In the water case, as reported by Thoroddsen *et al.* (2004), this ratio increases with increasing impact Reynolds number. Figure 14(*b*) shows an example of the high-speed ejecta observed for a sphere impacting onto water where the ejecta emerges 20 μs from impact. Despite the different time scales between the (compressible) granular case and the (incompressible) water case, we note the remarkable similarity in the physical appearance of the two sheets in the later frames of figure 14(*a,b*). In the water case, the first jet seen is extremely thin (and subsequently bends down to hit the free surface) and is intimately connected with the incompressibility of the water, then the main ejecta emerges (see the fourth panel of figure 14*b*). In contrast, the granular material is compressible and this first jet is absent.

Figure 15 shows the emerging sheet velocity (measured over the first several frames) versus impact velocity. Here V_s increases with V_0 in an almost linear fashion, as shown by the fit to the data representing the median value of the normalized sheet velocity, $V_s/V_0 = 2.2$. We can also see from the data that V_s increases with D_0, albeit to a lesser degree than V_0. However, this is more readily seen in figure 16 where we plot the sheet velocity against initial packing fraction for a fixed impact velocity $V_0 = 4.5$ m s^{-1}. Here, we observe that the sheet velocities are approximately 40 % higher as the sphere diameter doubles from 25 to 50 mm. More significantly, though, we find that the sheet velocity is independent of the initial packing fraction for the range tested here from $\phi = 0.49$ to $\phi = 0.61$. The data for $V_0 = 9.5$ m s^{-1} included in figure 16 also shows that this independence of packing fraction holds at higher impact velocity.

https://doi.org/10.1017/jfm.2012.141 Published online by Cambridge University Press

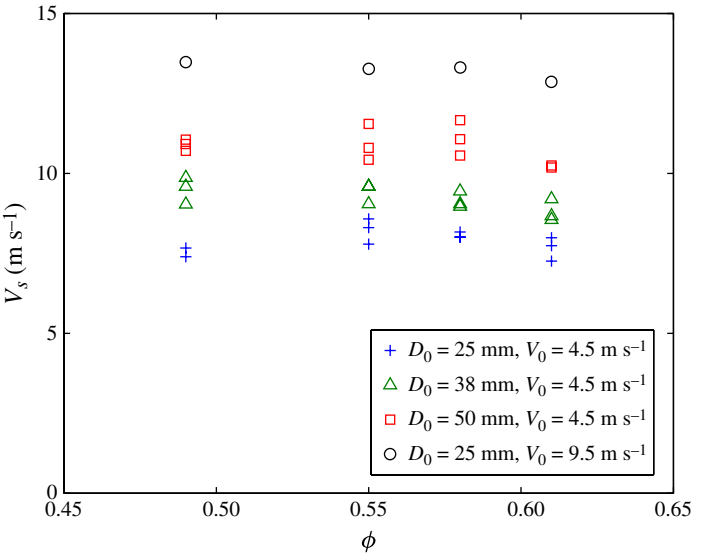


FIGURE 16. Sheet velocities V_s from experiments performed with fine grains ($d_b = 31$ μm) at different initial packing fractions, $\phi = 0.49$, 0.55, 0.58 and 0.61.

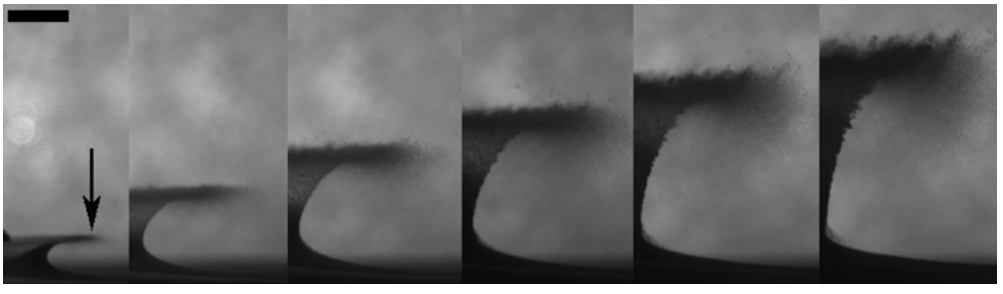


FIGURE 17. Frames from a high-speed video sequence showing the breakup of the sheet tip. The arrow in the first image indicates the tip of the sheet. Frames shown are taken at $t = 3.33$, 6.67, 10, 13.33, 16.67 and 20 ms from impact. The scale bar is 1 cm long. (Here $d_b = 31$ μm, $Fr = 4.8$, $\varrho = 6.4$ and $\epsilon = 1600$.)

6.2. *Sheet break-up and ejecta collapse*

Figure 17 shows an example of the evolution and break-up of the tip of the sheet. The sheet tip in the first frame is approximately 1 mm thick and grows substantially with time as shown in figure 18, indicating that the local porosity increases. It is also clear from this sequence that many grains are breaking away from the tip during the expansion of the ejecta as seen by the 'cloudy' formation below the sheet tip which becomes progressively larger. As discussed in § 2.4, the role of air drag becomes significant for these fine grains and is the likely cause of this cloud of particles.

During the latter stages of the ejecta (i.e. for $t > 10$ ms), the grains which break away from the tip are seen to be pulled down and back towards the ejecta edge. Figure 19 shows an example of this for the lowest packing fraction, $\phi = 0.49$, where the arrows indicate the flow of the grains. In the case of higher packing fractions,

https://doi.org/10.1017/jfm.2012.141 Published online by Cambridge University Press

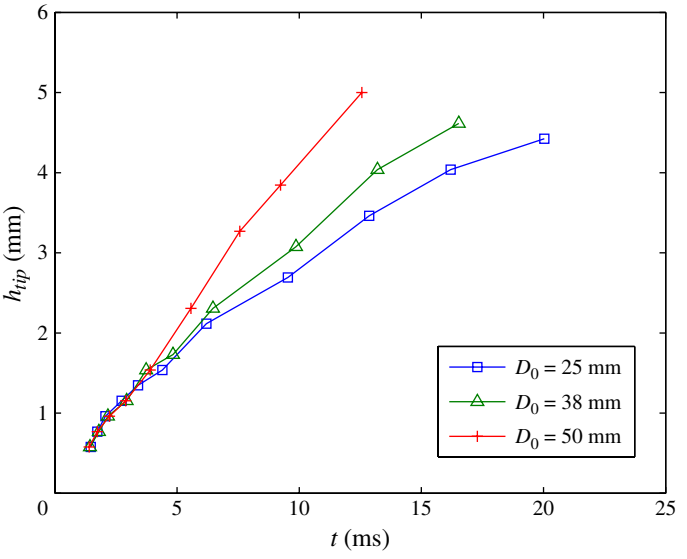


FIGURE 18. Sheet tip width h_{tip} versus time t for $\phi = 0.49$, $V_0 = 4.5$ m s^{-1} (with $\varrho = 6.4$, $Fr = 4.8$, 4.7 and 4.6).

the ejecta curtain breaks into clumps, thus forming a porous wall allowing grains to flow back through the ejecta (see supplementary video 5). The grains initially break from the tip of the ejecta sheet due to a confluence of air drag and local porosity and are then entrained back through the ejecta due to the vortex ring which occurs on the inside edge of the ejecta or 'curtain' (Barnouin-Jha & Schultz 1999) creating a pressure differential across the ejecta edge.

The fact that higher packing fractions lead to more porous ejecta, as shown by the snapshots in figure 20(*a*) may at first seem counterintuitive, but is natural when considering that the ejecta at low packing fractions is more susceptible to early collapse due to the air flow created by the vortex ring. Experiments in a vacuum would help to clarify the role of air in this particular aspect of the ejecta evolution. We can also see that the size of the ejecta diameters increases with the packing fraction as shown in figure 20(*b*) where the base diameter exhibits only a moderate increase from $D_e/D_0 = 2.5$ to 3 whilst the top diameter doubles from $D_t/D_0 = 3$ to 6 as the packing fraction increases from $\phi = 0.49$ to 0.61.

As such, at a qualitative level, we can conclude that while the packing fraction does not influence the early dynamics of the sheet for the fine grains, it does play a significant role in the later dynamics as evident from figures 18 and 19. This lack of influence during early time events was also observed for the emergence radius and ejecta velocities for the larger grains.

7. Ejecta evolution

7.1. *Neck propagation*

In order to quantitatively assess the growth of the ejecta, we track the most well-defined point of the ejecta, namely the neck radius, r_n which is the smallest horizontal distance from the edge of the ejecta to the sphere's axis of symmetry at impact, see figure 2 for a definition of this measurement and an example of how this measurement is made using image analysis. For the following analysis, we take $r_n(t = t_e) \equiv r_e$.

https://doi.org/10.1017/jfm.2012.141 Published online by Cambridge University Press

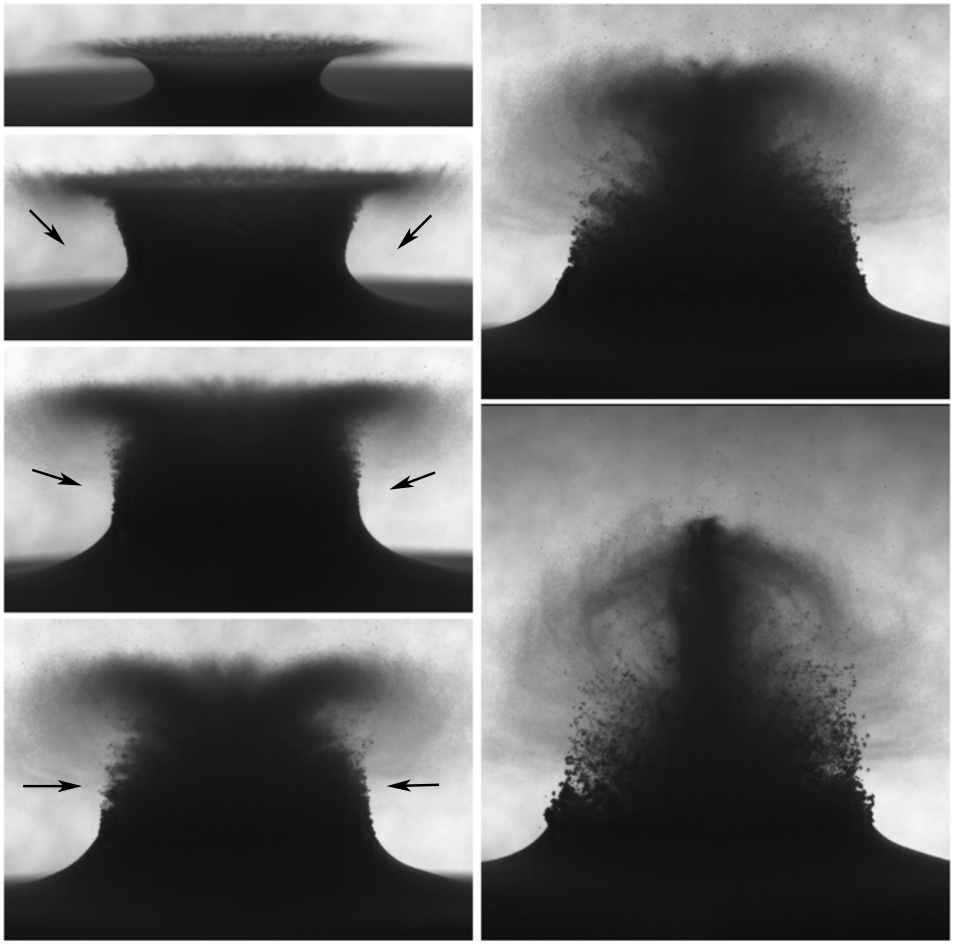


FIGURE 19. Sequence of images showing the break-up of the sheet and collapse of the ejecta for $d_b = 31$ μm ($D_0 = 25$ mm, $V_0 = 9.6$ m s^{-1}, $\phi = 0.5$, $Fr = 19.42$ and $\varrho = 6.2$). The arrows are included only as a guide to the direction of the flow of the grains in images 2–4. The images are taken at times $t = 3.5$, 9.8, 16, 24.3, 36.8 and 53.5 ms from impact. (See also supplementary video 4.)

For all of the materials tested in these experiments, including water, the neck can be tracked easily over the early times but becomes more difficult during the collapse (see, for example, figures 4 and 19). For most cases, therefore we track the neck until it is either no longer well defined or collapses back to the level of the bed. In certain cases, particularly for the finest grains, the ejecta neck evolution is distorted at later times due to a 'kink' in the ejecta edge which leads to a secondary neck close to the surface of the bed. In this circumstance, tracking is only performed up to this point to avoid a discontinuity in the radius versus time plots.

A comprehensive example of the ejecta neck tracking is shown in figure 21 for $d_b = 520$ μm glass beads ($\phi = 0.59$) showing plots of neck radius versus time, neck height versus time and neck height versus radius, respectively. Here, we can see that the early time evolution of both the normalized radius and height of the neck are essentially independent of the impacting sphere diameter, however, there are some

https://doi.org/10.1017/jfm.2012.141 Published online by Cambridge University Press

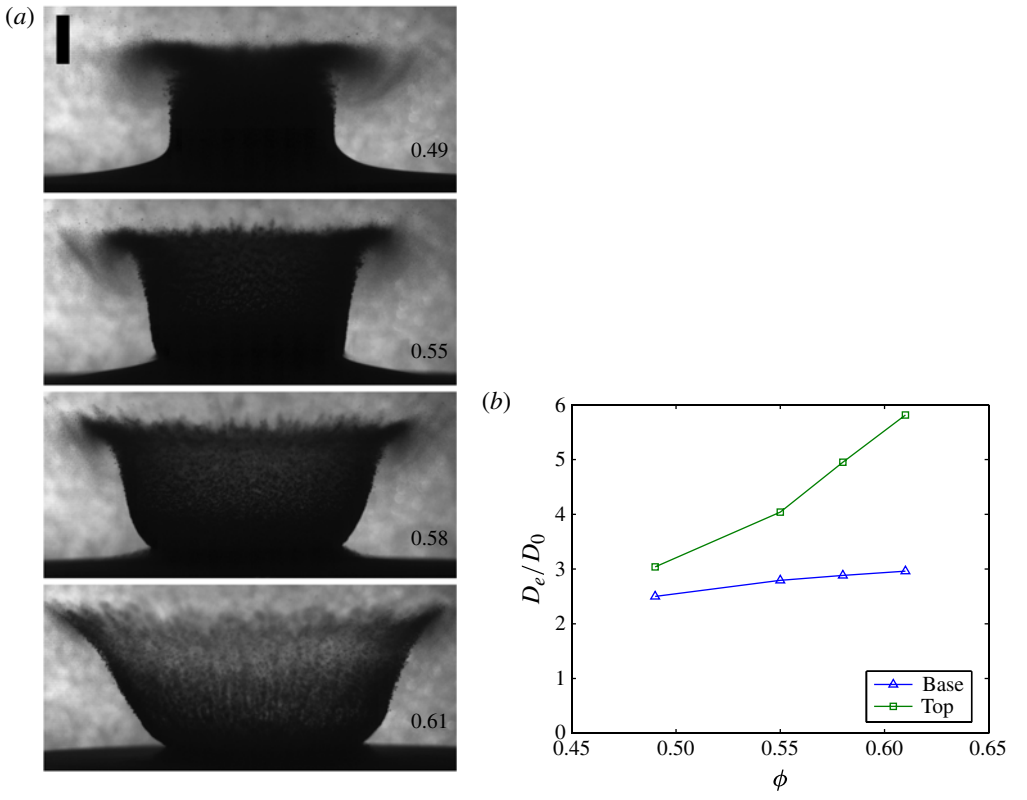


FIGURE 20. Influence of packing fraction on the overall ejecta shape. (*a*) Snapshots of the ejecta formed at 20 ms from impact for $d_b = 31$ μm glass beads with initial packing fractions (indicated on the right of the images) of $\phi = 0.49$, 0.55, 0.58 and 0.61. Here $D_0 = 25$ mm, $V_0 = 9.5$ m s^{-1} and $Fr = 19.2$. The scale bar is 2 cm long. (*b*) Base and top diameters D_e/D_0 of the ejecta shown in (*a*) versus packing fraction ϕ.

minor discrepancies during the latter stages during the collapse. This is also seen in experiments at a higher packing fraction ($\phi = 0.63$) where the dynamics are qualitatively similar, but we do observe some notable differences such as a 25 % increase in the maximum height reached where $h_{n,max}/D_0 \sim 0.5$ for $\phi = 0.63$ compared with $h_{n,max}/D_0 \sim 0.4$ for $\phi = 0.59$. There is also a slight discrepancy between the collapse times for sphere diameters $D_0 = 25$ mm and $D_0 = 38$ mm for the higher packing fractions.

7.2. *Scaling the early time ejecta growth*

Using the scalings $r' = (r_n - r_e)/D_0$ and $\tau = (t - t_e)V_0/D_0$, we seek power-law fits of the form $r' \sim C\tau^{\beta}$ for the early time evolution of the ejecta when $h_n \leqslant h_{n,max}$ and $\mathrm{d}h_n/\mathrm{d}t > 0$ (i.e. when the neck is still rising) which we take to be the true 'expansion' phase with the 'collapse' phase occurring for $h_n < h_{n,max}$ and $\mathrm{d}h_n/\mathrm{d}t < 0$. We also need to ensure that the container geometry does not become significant in the fitting, so we also restrict our fits to times $tV_0/D_0 < 4$, 2.6 and 2 for $D_0 = 25$, 38 and 50 mm, respectively. An example of this fitting procedure is presented in figure 22 for two different packing fractions, showing that the higher packing fraction results in a slightly faster expansion of the ejecta with $r' \sim \tau^{0.62}$ for $\phi = 0.63$ compared

https://doi.org/10.1017/jfm.2012.141 Published online by Cambridge University Press

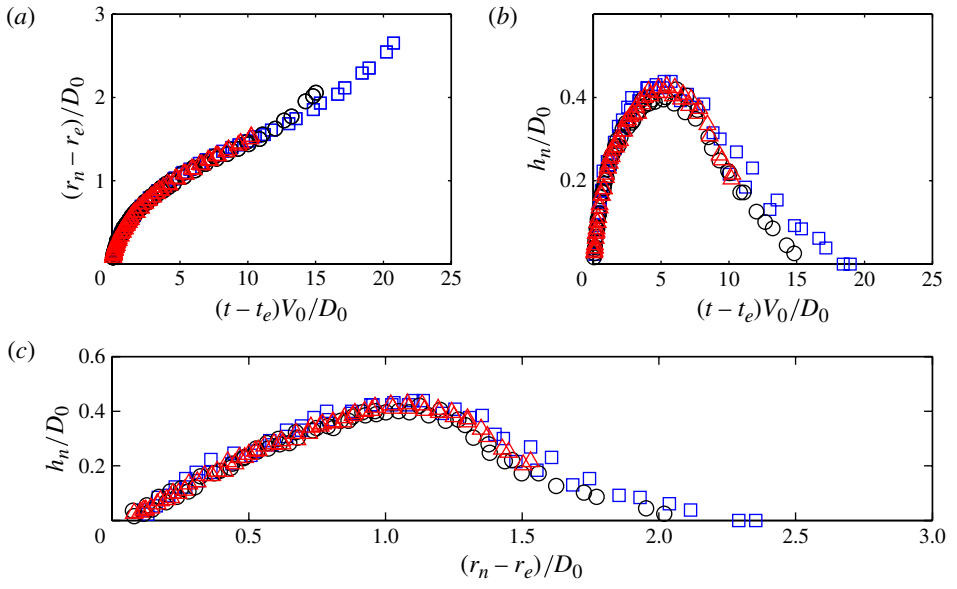


FIGURE 21. (*a*) Ejecta neck radius $(r_n - r_e)/D_0$ versus time from impact $(t - t_e)V_0/D_0$. (*b*) Ejecta neck height h_n/D_0 versus time from impact $(t - t_e)V_0/D_0$. (*c*) Ejecta neck height h_n/D_0 versus ejecta neck radius $(r_n - r_e)/D_0$. $d_b = 520\,\mu$m glass beads, $V_0 = 4.5$ m s^{-1}, $\phi = 0.59$ ($\varrho = 5.3$, $Fr = 4.8$, 4.7 and 4.6). Symbols indicate sphere diameter: $D_0 = 25$ mm (blue squares), $D_0 = 38$ mm (black circles) and $D_0 = 50$ mm (red triangles).

with $r' \sim \tau^{0.58}$ for $\phi = 0.59$. These power-law type evolutions are far from the quadratic evolution that was predicted by Deboeuf *et al.* (2009). We propose that this is due to the temporal resolution of our experimental measurements and the time frame of the fitting rather than a qualitative difference in the behaviour of the ejecta. We note again that their quadratic-type ejecta growth was predicted through fitting to their model rather than from direct experimental measurements. In fact, at later times with $(t - t_e)V_0/D_0 > 10$, we observe a slight acceleration in the expansion of the ejecta towards the collapse which can be approximated reasonably well with a quadratic polynomial. Full results from fitting the simple power-law scaling to all of the data sets for fixed impact velocity of $V_0 = 4.5$ m s^{-1} are presented in figure 23. Immediately we see that the power-law exponent is increasing monotonically with the packing fraction for all of the materials and, in addition, we observe two distinct sets within the data: one for the glass beads and one for the coarse sands. This data then suggests that we must also take the shape and size distributions into account since the median size of the sands are within the ranges of the glass beads. A simple regression analysis shows that $\beta \propto \phi^{0.7}\Delta S^{-0.05}C_{HS}^{-0.2}$, where $\Delta S = d_{90} - d_{10}/d_{50}$ is a size distribution factor and C_{HS} is the circularity measurement from § 2, showing the relative strength of the influence of these characteristics and that the packing fraction is the most important.

In particular, we note that for the lowest packing fraction of $\phi = 0.49$ achieved for the smallest grains, the exponent $\beta = 0.49$ indicating that the neck radius scales approximately with the square root of time, i.e. $r_n \sim t^{1/2}$, which was previously noted for the radial growth of the neck during drop impact onto liquid films (Weiss & Yarin 1999). This approach to fluid-like growth of the ejecta may result from a confluence of

https://doi.org/10.1017/jfm.2012.141 Published online by Cambridge University Press

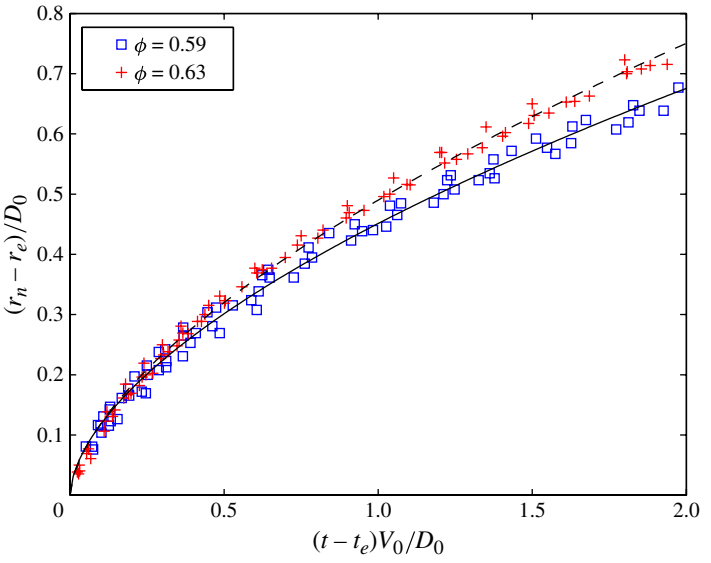


FIGURE 22. Early time data for neck radius $(r_n - r_e)/D_0$ versus time $(t - t_e)V_0/D_0$ with $\tau \leqslant 2$ for $d_b = 520$ μm glass beads, $\phi = 0.59$ and 0.63. The solid and dashed lines indicate power-law fits to the data with exponents of 0.58 and 0.615, respectively.

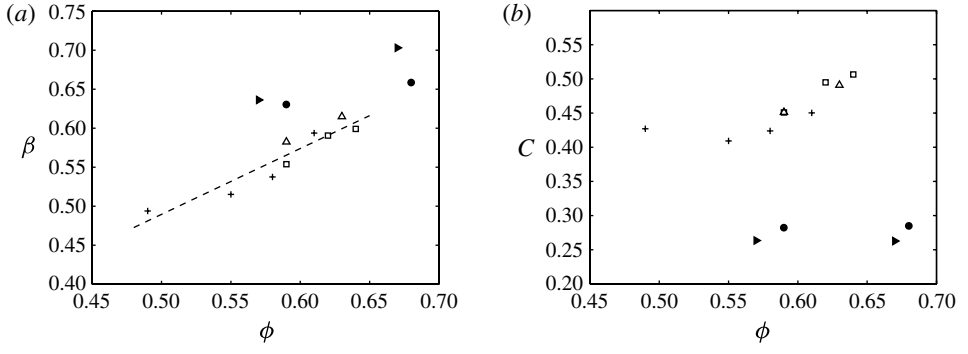


FIGURE 23. (*a*) Exponents derived from power-law fits β to the early time ($\tau \leqslant 2$) radial growth for a fixed impact velocity ($V_0 = 4.5$ m s^{-1}, $Fr = 6.4$, 7.4 and 9.1) and varying packing fraction ϕ ($4.6 \leqslant Dr \leqslant 6.4$). (*b*) Coefficients C corresponding to exponents in (*a*). Symbols: (+) glass beads, $d_b = 31$ μm; (□) glass beads $d_b = 178$ μm; (△) glass beads, $d_b = 520$ μm; (▷) beach sand, $d_b = 524$ μm; and (○) desert sand, $d_b = 310$ μm.

effects such as the increased role of air drag for the fine grains (see § 2.4) and possible role of minute capillary bridges which may be more profound for the small grains with low packing fractions (Royer *et al.* 2009). For discussion of granular viscosity, we refer the reader to § 8.1.

Figure 24 shows the power-law exponent, β, derived from fitting to 144 experimental trials plotted against the impact kinetic energy of the sphere, KE_0 spanning four orders of magnitude. The expansion exponents, β, for all of the experiments lie within the range $0.45 \leqslant \beta \leqslant 0.75$. For the finest grains at the lowest

https://doi.org/10.1017/jfm.2012.141 Published online by Cambridge University Press

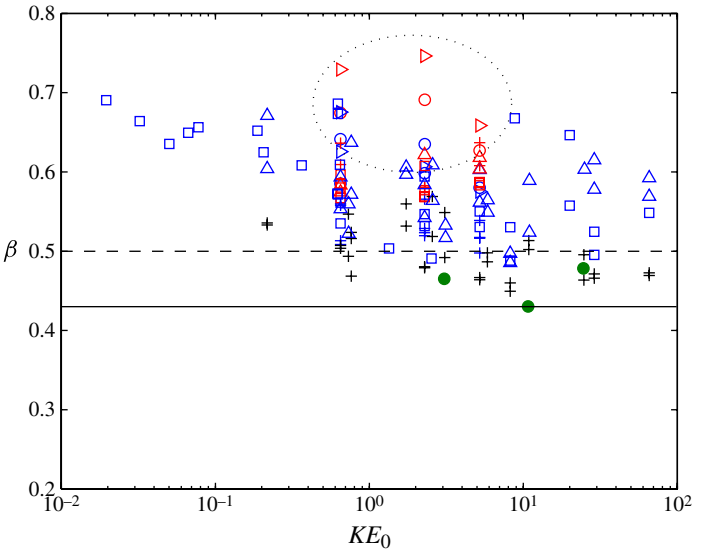


FIGURE 24. Power-law exponents, β, versus impact kinetic energy, KE_0. The dashed line is $\beta = 0.5$ (Weiss & Yarin 1999) and the solid line is $\beta = 0.43$ (Cossali *et al.* 2004). The symbols indicate packing fraction (black, $\phi \leqslant 0.55$; blue, $0.58 \leqslant \phi \leqslant 0.62$; red, $\phi > 0.63$) and material: (+) glass beads, $d_b = 31$ μm; (□) glass beads $d_b = 178$ μm; and (△) glass beads, $d_b = 520$ μm. The green filled circles represent data for water. The dotted ellipse encompasses data points for the coarse sands.

packing fractions, the temporal evolution of the ejecta radius scales as $r' \sim \tau^{0.5\pm0.05}$, i.e. exhibiting an approximate square-root dependence on time. For direct comparison, data for the expansion of water ejecta have been included in figure 24 (green circles), which fall between the solid and dashed lines which represent the values $\beta = 0.43$ and $\beta = 0.5$ which were determined by Weiss & Yarin (1999) and Cossali *et al.* (2004) for liquid drops impacting liquid pools and films, respectively. Many of our data points for the finest grains, with $KE_0 > O(1)$, also fall within this range, i.e. $0.43 \leqslant \beta \leqslant 0.5$. This finding, together with the fact that the ejecta is preceded by a sheet structure further reinforces the emergence of true fluid-like characteristics of the granular material.

8. Discussion and conclusions

8.1. *Granular viscosity*

The absence of a well-defined granular viscosity makes a direct comparison with the liquid case difficult; however, various models have been proposed which we will now consider. Following Jop, Forterre & Pouliquen (2006) and Lacaze & Kerswell (2009), we may assume that the effective viscosity is proportional to the confining pressure but inversely proportional to the effective shear rate. Thus, assuming a typical hydrostatic pressure in the granular bed, $P \sim \rho_g g D_0$ and impact shear rate $\gamma \sim V_0/D_0$, then a simplistic model of viscosity is

$$\mu_{eff} \sim P/\gamma = \rho_g g D_0^2/V_0. \tag{8.1}$$

Under this model, we have effective viscosities $\mu_{eff} = O(1-10)$ Pa s for the impact velocities and sphere sizes used herein. Other forms of effective viscosities or 'friction

https://doi.org/10.1017/jfm.2012.141 Published online by Cambridge University Press

coefficients' for granular materials have been reported in the literature, notably the works of Savage and co-workers (Lun *et al.* 1984; Savage & Sayed 1984; Savage 1989) who presented results from shear cell experiments giving granular viscosities

$$\mu_{eff} \sim \rho_g d_b^2 V_0 f(\phi)/D_0, \tag{8.2}$$

where the function $f(\phi)$ diverges as the volume packing fraction approaches the critical packing fraction. Since f is a strong function of the packing fraction (Stickel & Powell 2005), which is not always known from our current experimental set-up, we seek to eliminate $f(\phi)$ from (8.2) using the pressure as the control parameter. Following Forterre & Pouliquen (2008), we note that $f(\phi) \propto P/(\rho_g d_b^2 \gamma^2)$, thus we find that (8.2) reduces to

$$\mu_{eff} \sim PD_0/V_0 \tag{8.3}$$

in which case, substituting the hydrostatic pressure $\rho_g g D_0$ for P, we recover (8.1). As such, in the absence of instantaneous measurements of the local packing fraction, equation (8.1) provides us with a more reliable estimate of the granular viscosity.

Other studies have also reported values of effective viscosities for granular medium and fluidized beds; an estimate of 2.2 Pa s was given for a bed of 475 μm glass beads by King, Mitchell & Harrison (1981) based on drag force calculations of a sphere falling through a fluidized bed; Grace (1970) derived $\mu_{eff} = 0.95$ Pa s for 500 μm glass beads from rising bubbles whilst Zeilstra (2007) determined effective viscosities of 0.6–0.9 Pa s from simulations based on a sphere falling through a bed of 500 μm particles with a bulk packing fraction $\phi = 0.6$. The parameters used in Zeilstra's calculations are close to those used in the experiments here for the large (520 μm) glass beads and are in reasonable agreement with the estimate based on (8.1) for high impact velocities, so as a first approximation we could take $\mu_{eff} \approx 1$ Pa s. Given the range of impact velocities used, this yields impact Reynolds numbers $Re_i = \rho_b V_0 D_0/\mu_{eff} \approx 100$–$1300$ for the largest glass beads used herein ($d_b = 520$ μm).

For an impact Reynolds number $Re_i = O(10^3)$ onto liquid pools, Thoroddsen *et al.* (2004) found normalized ejecta sheet velocities of $V_s/V_0 \sim 5$. At the earliest times, and for the highest impact velocities with similar values of Re_i, we found grain ejection velocities $V_g/V_0 \leqslant 5$ for the 520 μm glass beads which are of the same order of magnitude as the water ejecta sheets observed by Thoroddsen and colleagues. However, for the fine grains, $d_b = 31$ μm, where we observed the 'sheets', the normalized velocities $V_s/V_0 \approx 2$ which are lower than those seen for the liquid case. Experimental data to determine effective viscosities for these fine grains would certainly help to clarify the differences between the liquid and granular cases.

Estimates of $\Delta\phi$, the change in local packing fraction, at the moment of impact would be insightful with regards to the fluidization (or compaction) that may occur locally around the impact site. Royer *et al.* (2007) estimate that this may vary by up to 5 %, which could then lead to a large variation in effective viscosity (Stickel & Powell 2005; Forterre & Pouliquen 2008). Furthermore experiments investigating the temporal evolution of the crown during drop and sphere impacts onto viscous liquid pools would aid in our understanding of the relationship between μ_{eff} and ϕ.

8.2. *Conclusions*

In conclusion, we have performed an experimental study of the shape and speed of the ejecta following the impact of a sphere onto a granular bed. We have examined individual grain ejection velocities during the 'early stage' ejecta flow. The first motions from the bed occur within the first few milliseconds after impact and this

https://doi.org/10.1017/jfm.2012.141 Published online by Cambridge University Press

time, t_e, was found to be inversely proportional to the impact shear rate, V_0/D_0. For large grain sizes, the velocity distribution is measured as a function of the ejection angle and time from impact where, in general, the velocity decreases as the ejecta angle increases, i.e. the fastest grains tend to emerge with the lowest angles. We also observe an inverse proportionality between the ejecta velocity and the ejection time from impact, i.e. $V_g/V_0 \sim T^{-1}$ where $T = tV_0/D_0$, which coincides with scalings by Holsapple (1993) and Hermalyn & Schultz (2011) for this early stage ejecta. Some stark differences were observed between the near-spherical glass beads and the coarse sands where, for the latter, we found a narrower range of ejection velocities and a weaker dependence on both time and initial bed packing fraction. We have also proposed scalings for the mean ejection velocity in terms of the impact kinetic energy, with different scalings found for $KE_0 \lesseqgtr 5$. A comparison of our scalings with those previously reported was made showing that experimental conditions and the impactor-to-grain size ratio are important.

As the grain size was decreased, we observed a transition to a more fluid-like behaviour whereby the first ejecta appears in the form of a sheet whose velocity is approximately twice that of the impacting sphere, i.e. $V_s/V_0 \approx 2$. Surprisingly, the sheet velocity was found to be independent of the bulk packing fraction. During the later evolution of the ejecta curtain for the finest grains, we did however note a significant dependence on the bulk packing fraction in terms of the appearance and break-up of the sheet and ejecta with observations of grains being entrained back towards the ejecta edge due to the vortex ring inside of the ejecta curtain as proposed previously by Barnouin-Jha & Schultz (1999).

The ejecta neck evolution for all grains was found to exhibit a strong dependence on the bulk packing fraction for the spherical glass beads and approaches a $t^{1/2}$ scaling law with both decreasing grain size and with increasing impact kinetic energy, showing similarities to the neck evolution of liquid crown during drop impact experiments.

It is plausible that some basic features of the impact dynamics, e.g. the emergence radius and the grain (or sheet) ejecta velocities can be used as a crude method to deduce (or verify) some physical properties and characteristics of the granular material such as particle interlocking (resistance to shear) and effective bed viscosity. Further experiments in a reduced ambient pressure, in order to assess the influence of interstitial air and air drag on the ejecta evolution are the subject of ongoing investigation.

Acknowledgement

This work was partially supported by an Academic Excellence Alliance grant awarded by the KAUST office of Competitive Research Funds number 7000000028.

Supplementary videos are available at journals.cambridge.org/flm.

REFERENCES

AMBROSO, M. A., SANTORE, C. R., ABATE, A. R. & DURIAN, D. J. 2005 Penetration depth for shallow impact cratering. *Phys. Rev.* E **71**, 051305.

BARNOUIN-JHA, O. S. & SCHULTZ, P. 1999 Interactions between an impact generated ejecta curtain and an atmosphere. *J. Impact Engng* **23**, 51–62.

BELADJINE, D., AMMI, M., OGER, L & ALEXANDRE, V. 2007 Collision process between an incident bead and a three-dimensional granular packing. *Phys. Rev.* E **75**, 061305.

https://doi.org/10.1017/jfm.2012.141 Published online by Cambridge University Press

BOUDET, J. F., AMAROUCHENE, Y., BONNIER, B. & KELLAY, H. 2007 The granular jump. *J. Fluid Mech.* **413**, 413–431.

BOUDET, J. F., AMAROUCHENE, Y. & KELLAY, H. 2006 Dynamics of impact cratering in shallow sand layers. *Phys. Rev. Lett.* **96**, 158001.

CABALLERO, G., BERGMANN, R., VAN DER MEER, D., PROSPERETTI, A. & LOHSE, D. 2007 Role of air in granular jet formation. *Phys. Rev. Lett.* **99**, 018001.

CHENG, X., VARAS, G., CITRON, D., JAEGER, H. M. & NAGEL, S. R. 2007 Collective behaviour in a granular jet: emergence of a liquid with zero surface tension. *Phys. Rev. Lett.* **99**, 188001.

COLWELL, J. E., STURE, S., CINTALA, M., DURDA, D., HENDRIX, A., GOUDIE, T., CURTIS, D., ASHCOM, D. J., KANTER, M., KEOHANE, T., LEMOS, A., LUPTON, M. & ROUTE, M. 2008 Ejecta from impacts at 0.2–2.3 m s^{-1} in low gravity. *Icarus* **195**, 908–917.

COSSALI, G. E., MARENGO, M., COGHE, A. & ZHDANOV, S. 2004 The role of time in single drop splash on thin film. *Exp. Fluids* **36**, 888–900.

DEBOEUF, S., GONDRET, P. & RABAUD, M. 2009 Dynamics of grain ejection by sphere impact on a granular bed. *Phys. Rev.* E **79**, 041306.

EGGERS, J. & VILLERMAUX, E. 2008 Physics of liquid jets. *Rep. Prog. Phys.* **71**, 036601.

FORTERRE, Y. & POULIQUEN, O. 2008 Flows of dense granular media. *Annu. Rev. Fluid Mech.* **40**, 1–24.

GRACE, J. R. 1970 The viscosity of fluidised beds. *Can. J. Chem. Engng* **48**, 30.

GOLDMAN, D. I. & UMBAHNOWAR, P. 2008 Scaling and dynamics of sphere and disk impact into granular media. *Phys. Rev.* E. **77**, 021308.

HAPGOOD, K. P., LISTER, J. D., BIGGS, S. R. & HOWES, T. 2002 Drop penetration into porous powder beds. *J. Colloid Interface Sci.* **253**, 353–366.

HARTMANN, W. K. 1985 Impact Experiments 1. Ejecta velocity distributions and related results from regolith targets. *Icarus* **63**, 69–98.

HERMALYN, B. & SCHULTZ, P. H. 2010 Early-stage ejecta velocity distribution for vertical hypervelocity impacts into sand. *Icarus* **209**, 866–870.

HERMALYN, B. & SCHULTZ, P. H. 2011 Time-resolved studies of hypervelocity impacts into porous particulate targets: effects of projectile density on early-time coupling and crater growth. *Icarus* **216**, 269–279.

HOLSAPPLE, K. A. 1993 The scaling of impact processes in planetary sciences. *Annu. Rev. Earth Planet. Sci.* **21**, 333–373.

HOUSEN, K. R. & HOLSAPPLE, K. A. 2011 Ejecta from impact craters. *Icarus* **211**, 856–875.

JOP, P., FORTERRE, Y. & POULIQUEN, O. 2006 A constitutive law for dense granular flows. *Nature* **441**, 727–730.

VON KANN, S., JOUBAUD, S., CABALLERO-ROBLEDO, G. A., LOHSE, D. & VAN DER MEER, D. 2010 Effect of finite container size on granular jet formation. *Phys. Rev.* E **81**, 041306.

KING, D. F., MITCHELL, F. R. G. & HARRISON, D. 1981 Dense phase viscosities of fluidised beds at elevated pressures. *Powder Technol.* **28**, 55–58.

LACAZE, L. & KERSWELL, R. 2009 Axisymmetric granular collapse: a transient 3D test of viscoplasticity. *Phys. Rev. Lett.* **102**, 108305.

LOHSE, D., BERGMANN, R., MIKKELSEN, R., ZEILSTRA, C., VAN DER MEER, D., VERSLUIS, M., VAN DER WEELE, K., VAN DER HOEF, M. & KUIPERS, H. 2004 Impact on soft sand: void collapse and jet formation. *Phys. Rev. Lett.* **93** (19), 198003.

LUN, C. K., SAVAGE, S. B., JEFFREY, D. J. & CHEPURNIY, N 1984 Kinetic theories for granular flow: inelastic particles in Couette flow and slightly inelastic particles in a general flow field. *J. Fluid Mech.* **140**, 223.

MARSTON, J. O., SEVILLE, J. P. K., CHEUN, Y.-V., INGRAM, A., DECENT, S. P. & SIMMONS, M. J. H. 2008 Effect of packing fraction on granular jetting from solid sphere entry into aerated and fluidised beds. *Phys. Fluids* **20**, 023301.

MICHIKAMI, T., MORIGUCHI, K., HASEGAWA, S. & FUJIWARA, A. 2007 Ejecta velocity distribution for impact cratering experiments on porous and low strength targets. *Planet. Space Sci.* **55**, 70–88.

https://doi.org/10.1017/jfm.2012.141 Published online by Cambridge University Press

MOBIUS, M. E. 2006 Clustering instability in a freely falling granular jet. *Phys. Rev.* E **74**, 051304.

O'KEEFE, J. D. & AHRENS, T. J. 1985 Impact and explosion crater ejecta, fragmentation size, and velocity. *Icarus* **62**, 328–338.

ROYER, J. R., CORWIN, E. I., CONYERS, B., FLIOR, A., RIVERS, M. L., ENG, P. J. & JAEGER, H. M. 2008 Birth and growth of a granular jet. *Phys. Rev.* E **78**, 011305.

ROYER, J. R., CORWIN, E. I., ENG, P. J. & JAEGER, H. M. 2007 Gas-mediated impact dynamics in fine-grained granular materials. *Phys. Rev. Lett.* **99**, 038003.

ROYER, J. R., EVANS, D. J., OYARTE, L., GUO, Q., KAPIT, E., MOBIUS, M. E., WAITUKAITIS, S. R. & JAEGER, H. M. 2009 High-speed tracking of rupture and clustering in freely falling granular streams. *Nature* **459**, 1110–1113.

SAVAGE, S. B. 1989 Flow of granular materials. In *Theoretical and Applied Mechanics*, pp. 241–266. Elsevier.

SAVAGE, S. B. & SAYED, M. 1984 Stresses developed by dry cohesionless granular materials sheared in an annular shear cell. *J. Fluid Mech.* **142**, 391–430.

SEGUIN, A., BERTHO, Y. & GONDRET, P. 2008 Influence of confinement on granular penetration by impact. *Phys. Rev.* E **78**, 010301.

STEPHENSEN, R. 2000 Shallow foundations. In *Practical Foundation Engineering Handbook*, 2nd edn (ed. R. Brown), pp. 135–164. McGraw-Hill Publishing.

STICKEL, J. J. & POWELL, R. L. 2005 Fluid mechanics and rheology of dense suspensions. *Annu. Rev. Fluid Mech.* **37**, 129–149.

THORODDSEN, S. T., ETOH, T. G., TAKEHARA, K. & TAKANO, Y. 2004 Impact jetting by a solid sphere. *J. Fluid Mech.* **499**, 139–148.

THORODDSEN, S. T. & SHEN, A. Q. 2001 Granular jets. *Phys. Fluids* **13** (1), 4–6.

THORODDSEN, S. T., THORAVAL, M.-J., TAKEHARA, K. & ETOH, T. G. 2011 Droplet splashing by a slingshot mechanism. *Phys. Rev. Lett.* **106**, 034501.

UEHARA, J. S., AMBROSO, M. A., OJHA, R. P. & DURIAN, D. J. 2003 Low-speed impact crater in loose granular media. *Phys. Rev. Lett.* **90**, 194301.

UMBANHOWAR, P. & GOLDMAN, D. I. 2010 Granular impact and the critical packing state. *Phys. Rev.* E **82**, 010301.

DE VET, S. J. & DE BRUYN, J. R. 2007 Shape of impact craters in granular media. *Phys. Rev.* E. **76**, 041306.

WALSH, A. M., HOLLOWAY, K. E., HABDAS, P. & DE BRUYN, J. R. 2003 Morphology and scaling of impact craters in granular media. *Phys. Rev. Lett.* **91** (10), 104301.

WEISS, D. A. & YARIN, A. L. 1999 Single drop impact onto liquid films: neck distortion, jetting, tiny bubble entrapment, and crown formation. *J. Fluid Mech.* **385**, 229–254.

YAMAMOTO, S., KADONO, T., SUGITA, S. & MATSUI, T. 2005 Velocity distributions of high-velocity ejecta from regolith targets. *Icarus* **178**, 264–273.

YAMAMOTO, S., WADA, K., OKABE, N. & MATSUI, T. 2006 Transient crater growth in granular targets: an experimental study of low velocity impacts into glass sphere targets. *Icarus* **183**, 215–224.

ZEILSTRA, C. 2007 Granular dynamics in vibrated beds. PhD thesis, University of Twente.

https://doi.org/10.1017/jfm.2012.141 Published online by Cambridge University Press